A Detailed Study of the Complex
Line-Emission Regions in the Radio Galaxy 3C 34

Mark J. Neeser[1], Klaus Meisenheimer, and Hans Hippelein

Max-Planck-Institut für Astronomie, Königstuhl 17, 69117 Heidelberg, Germany

ABSTRACT

We present the results of an extensive Fabry-Perot investigation of the extended line-emission gas surrounding powerful radio galaxies. High spatial ($\lesssim 1''\!.4$) and kinematical ($400\,\mathrm{km\,s^{-1}}$) resolution observations of the [O II]$\lambda3727$ emission-line of the powerful, double radio source 3C 34 (z=0.689) are given. We present evidence that anisotropic radiation emanating from a hidden AGN is responsible for photoionizing a line-emission region extending more than $120\,\mathrm{kpc}$. This is indicated by the distinctively bi-conical morphology of 3C 34's [O II] gas. A number of line-emission components may also show various degrees of 'shadowing' outward from the central ionizing source. A simple photoionization model is used to show that this interpretation is energetically viable on these length scales. The luminosity of the hidden central AGN, necessary to account for the observed [O II] luminosity, is compatible with that of a typical 3CR quasar at a similar redshift. Although this interpretation can account for the excitation and most of the unique shape of the warm gas, it is insufficient to explain the velocity and line-width structures observed with our Fabry-Perot. Therefore, we also propose that the illuminated medium surrounding 3C 34 is the result of gas swept up by the lateral expansion and backflow of the radio source lobes.

Subject headings: galaxies: active — galaxies: individual (3C 34) — galaxies: ISM — galaxies: emission-lines

---

[1]e-mail: neeser@mpia-hd.mpg.de

1.   Introduction

The distant radio galaxy 3C 34 (z=0.6897) has a remarkable extended emission-line region, whose size (140 kpc) and brightness make it ideally suited to an in depth morphological and kinematical investigation. A number of high quality radio maps of 3C 34, primarily at 6 cm and 20 cm, can be found in the literature (*e.g.* Jenkins et al. 1977; Garrington et al. 1991; Neff et al. 1995; Johnson et al. 1995). These maps show this powerful radio galaxy to be a relatively symmetric, edge-brightened, 45″ classical double. The first definitive optical identification of 3C 34 was made by Riley et al. 1980, who detected a faint, diffuse object located between the two brightest radio features. Although the detection of a strong [O II]λ3727 emission-line was sufficient to determine the redshift of this galaxy, the only other feature evident on the spectra of Spinrad 1982 is a very weak [Ne III]λ3869 line. The r_s-filter and intermediate-band imaging of McCarthy et al. 1995 reveal a galaxy in a rich compact cluster environment, and an extended region of high surface brightness [O II]λ3727 that is aligned with the radio source. This is also evident in the higher spatial resolution narrow-band [O II] and I-band continuum images presented by Johnson et al. 1995. Follow-up long-slit spectroscopy (McCarthy et al. 1996) of moderate quality detected both [O II]λ3727 and [O III]λ5007 emission, and allowed a rough velocity profile to be fit to the central region of 3C 34.

3C 34 is a spectacular example of the positional coincidence between the optical line-emission and the radio source axis, discovered to be a common phenomena in powerful, high redshift radio galaxies (McCarthy et al. 1987; Chambers et al. 1987). The combination of the novelty of this 'alignment effect', with the often spectacular morphologies of extended emission-line regions, and their potential effects on the evolution and formation of radio galaxies, attracted lively debate, little consensus, and a large number of possible explanations for this phenomenon. However, since the line-emission regions in high redshift radio galaxies, by virtue of their large intrinsic luminosities and large spatial extents, provide one of the best methods for probing the warm gas at early epochs and across a broad range of redshifts, the importance of understanding the alignment effect cannot be understated. Since this phenomena arises in extended, highly dynamic gas, an investigation that combines well-resolved morphologies with kinematics would go far in shedding new light on the question of the origin of the line-emission gas, its excitation, and the cause of the alignment effect. We therefore began an in depth survey of the [O II]λ3727 line-emission in 11 radio galaxies ($0.45 \lesssim z \lesssim 1.1$) using a Fabry-Perot etalon. This instrument produces seeing-limited maps of both the morphological and kinematical structure of these line-emission regions. We continue with the presentation of this data by describing our results for the powerful, high redshift radio galaxy 3C 34.

This paper has been organized as follows. In the first section we present the observations and the data reduction. In section 3 we give a qualitative description of the emission-line and continuum morphologies, and the kinematics of the [O II] gas. Our interpretation of this data, in terms of a model to account for the ionization, origin, and kinematics of the warm gas in 3C 34, is discussed in section 4. This section concludes with an account of alternative

models. In order to compute physical sizes, 'proper' distances, and luminosities, a standard Friedmann-Robertson-Walker cosmology with a zero cosmological constant, $H_o=50\,km\,s^{-1}\,Mpc^{-1}$, and $q_o=0.5$, have been assumed throughout this paper. At the redshift of 3C 34 this results in a luminosity distance of $1.44 \times 10^{28}\,cm$ and an angular scale of $7.94\,kpc\,arcsec^{-1}$.

2. Observations

2.1. Observations of 3C 34

The Fabry-Perot and continuum images of 3C 34 were obtained on Sept. 1991 and Sept. 1992, respectively, at the prime focus focal reducer of the 3.5 m telescope on Calar Alto, Spain. The [O II]λ3727 imaging spectroscopy was done with a GEC chip having 22.5μm pixels, giving a 'plate' scale of 0$''$49/pixel. We observed 3C 34 at 10 different wavelength settings between 6270Å and 6324Å, separated by 6Å steps. Multiple exposures of 1200 seconds each were made at every wavelength step, and resulted in 22 individual Fabry-Perot images. This allowed complete coverage of the redshifted [O II]λ3727 line. An interference order 30, corresponding to an instrumental profile width FWHM of $\Delta\lambda$=8.3Å, was chosen to give a spectral resolution of $395\,km\,s^{-1}$. The resulting [O II] images of 3C 34 ranged in seeing from 1$''$1 to 1$''$7 FWHM, with a median value of 1$''$3. To investigate the continuum morphology, as well as subtract its contribution to the [O II] images, line-free continuum exposures were obtained immediately redward of our [O II]λ3727 observations. These were taken at λ=6811Å ($\Delta\lambda$=180Å), and correspond to λ_o=4033Å ($\Delta\lambda_o$=107Å) in the rest frame of the radio galaxy. A total of five exposures of 500 seconds each were obtained in this continuum filter using a TEK chip with 24μm pixels and a resulting image scale of 0$''$53/pixel.

2.2. Data Reduction

Since the reduction procedures unique to Fabry-Perot (FP) images are described in detail in Meisenheimer & Hippelein 1992, we will give only a brief summary of the processing steps applied to the data obtained for 3C 34. The initial reduction followed that of standard CCD data processing: bias subtraction, dark current correction, flat fielding done using dome flat exposures obtained at the wavelength of each Fabry-Perot science image, and the removal of cosmic ray events. Further reduction steps, peculiar to FP imaging and necessary to extract the kinematical information, are briefly summarized.

(i) Night sky emission-lines (in particular, OI at λ≃6300Å) cause a 'ring' of enhanced background on each Fabry-Perot image at wavelengths shortward of the observed wavelength. An interpolation of the background pixels (defined from the local background level of each frame and a user-given σ–clipping) resulted in a fit of the radial profile of this emission. This background fit was smoothed in its radial and azimuthal directions and subtracted from each Fabry-Perot frame.

(ii) The alignment and relative scaling of all frames was based on a comparison of positions, profiles and intensities of 10 field stars of intermediate brightness. Since our subsequent spectral analysis of the [O II] line was done over the entire range of sampled wavelengths and included 22 individual frames, the degree of alignment between individual images needed to be better than $\sim 0\rlap{.}''05$ to prevent a cumulative positional error from becoming unacceptably large. This level of alignment was ensured by computing frame differences, examining the residual star images, and interactively adjusting the frame shift, rotation, and scale, until the desired overlap accuracy was achieved. The relative intensity scaling of each Fabry-Perot frame, with respect to the reference image, followed by requiring that the average continuum source in the field (*i.e.* the 10 reference field stars) showed a flat spectrum across the wavelength range covered by the Fabry-Perot images. This allowed us to adequately reduce the influence of possible intensity gradients, characteristic of some late-type stellar spectra, in our determination of the normalization constant.

(iii) In order to transform all of the Fabry-Perot and continuum images to a common positional reference frame and a common effective point spread function (PSF), a two-by-two pixel rebinning was done for all exposures. The FWHM chosen for the PSF convolution ($1\rlap{.}''65$) was somewhat broader than the FWHM of the Fabry-Perot image having the worst seeing. The result of this rebinning was a set of images with zero positional offsets, identical intensity normalizations, identical circular PSFs, and a pixel scale of $0\rlap{.}''247$ pixel^{-1}. To obtain pure line-emission images the scaled and rebinned continuum frame was subtracted from each Fabry-Perot image.

(iv) These line-emission images were then stacked into a cube with wavelength as the third dimension. A fit of a single Gaussian profile was made through this cube at each pixel of the source, when the total line flux in each pixel exceeded a given threshold. The output of this spectral fitting analysis consisted of six 2-dimensional frames containing the peak amplitude of the line-emission, the wavelength value of this maximum, its e-folding width, and the rms errors associated with each of these parameters. From these fit parameters we were then able to compute the the relative velocity and the FWHM of the [O II]$\lambda3727$ line-emission at each pixel.

(v) Standard aperture photometry techniques were used to determine the counts–to–flux conversions from the observed standard star, and used to photometrically calibrate the continuum and FP images. Observations of the calibration standard were only made at the central FP wavelength ($\lambda=6294$Å) setting. However, since the remaining Fabry-Perot images were scaled to this wavelength (step (ii)), a calibration of the entire [O II]$\lambda3727$ line could be made. Using a generalized non-linear least-squares curve these flux points were fit to a Gaussian profile by varying the amplitude, central wavelength, and standard deviation of the Gaussian profile until an optimum fit, indicated by a minimized χ^2, was achieved. The outermost wavelength points were assumed to sample only the continuum emission from the source, and hence the fit was forced to be flat at this level. The total line-emission

flux was then calculated by assigning the absolute value of the flux density obtained for the central wavelength frame to the amplitude of the fit, and integrating the profile across the line. The statistical uncertainty assigned to the flux density and the profile width were found by separately varying the amplitude and the standard deviation of the Gaussian fit, respectively, until χ^2 was increased by one for each parameter. We estimate a typical formal uncertainty in our determination of the total [O II] line flux to be better than 20%. Due to the Galactic latitude of 3C 34 ($b \simeq -31°$), no extinction correction for Galactic reddening was necessary (E(B–V) < 0.03, Burstein & Heiles 1982).

3.   Results

3.1.   Morphology

The continuum and line-emission images of 3C 34 are shown as contour maps in figure 1 with the components discussed in the text labelled.

3.1.1.   Emission–Line Morphology

The [O II] line-emission morphology of 3C 34 is spectacular in both its extent and complexity. The continuum-subtracted [O II]λ3727 grayscale image of 3C 34 is shown in the top panel of figure 2. The central region is dominated by a double-lobed, high surface brightness feature characterized by the two emission peaks, A and B. We identify the brightest line-emission source (component A) with the radio galaxy, as it is displaced by only $\simeq 0\rlap{.}''3$ to the southwest of the central continuum source (see figures 1 and 3). In contrast, the line-emission peak at B is not associated with an underlying continuum source, and has an intensity cross-section that is indistinguishable from a stellar profile. A further difference between these two components is that the line-emission falls off steeply and ends abruptly to background flux levels toward the northeast of source B. The outer end of component A levels off and merges with a faint finger line-emission extending a further $2\rlap{.}''5$ beyond the southwestern end of this central [O II] component (see figure 3).

Almost directly to the west of component A lies another [O II] knot, component a. This source is at the apex of a unique V-shaped structure that opens toward the west, away from the radio galaxy center. It is particularly interesting that these two fingers of emission extend symmetrically from either side of the line connecting component a with the central radio galaxy, and also lie on either side of the central axis of the western radio lobe.

The eastern side of 3C 34 is the most extended and contains two further knots of line-emission, components b and c. Component b sits close to the double-lobed central feature, but marks a sudden change in direction by being almost perpendicular to the major axis defined by components A and B. Further westward from component b is the strongly asymmetrical knot c, whose contours

are noticeably compressed in the direction toward the radio galaxy center, and stretched in the opposing direction. This is particularly evident in the intensity cross-section of the eastern region shown in figure 3. These steep contours also continue around to the south of component c, but strongly fan out toward the west and north of this source. On this side the surface brightness of component c gradually diminishes to the fainter flux levels of the eastern line-emission region.

The projected [O II] line-emission region of 3C 34 extends for an uninterrupted $18''$ or 144 kpc, placing it among the largest extended emission-line regions known. Despite this large overall size, the lateral extent of the line-emission is quite narrow and never exceeds roughly $5''(41$ kpc), giving 3C 34 an axial ratio of almost 1:4. It is interesting to note the overall twisted morphology of the emission-line region. Beyond the rather well-defined position angle of the central sources (components A and B), the fainter more extended line-emission to the east and west undergo radical changes in direction. Considering both the differences in surface brightness and orientation, the overall line-emission in 3C 34 can be divided into three distinct regions; the *central* component dominated by sources A and B, and the two outer *eastern* and *western* regions distinguished by knots b and c, and knot a, respectively.

To improve the objectivity in determining the position angle of our line-emission data we included only those pixels above a flux threshold of $3\sigma_{\mathrm{sky\,rms}}$, and computed the flux-weighted first and second moments of the [O II] image. This gave a position angle of $103° \pm 1°$for the extended emission-line region of 3C 34. Comparing this to the orientation of the radio emission, as measured along the line connecting the outermost hotspots, 3C 34 is moderately well-aligned with $\Delta\mathrm{PA} = 18°$.

The pure [O II]$\lambda 3727$ line-emission from 3C 34, within a circular aperture of $9''\!.6$ radius, is $2.23 \times 10^{-14}\,\mathrm{erg\,s^{-1}cm^{-2}}$. For the cosmological parameters defined in the introduction this translates to a total [O II]$\lambda 3727$ luminosity of

$$L_{[OII]} = 5.8 \times 10^{43} \quad \mathrm{erg\,s^{-1}}.$$

If we assume that the observed [O II] emission originates in a plasma with temperatures of about 10^4 K, in which the most abundant oxygen ion is O^+, then the gas density can be related to the [O II]$\lambda 3727$ line luminosity by

$$L_{[\mathrm{OII}]} = 2.3 \times 10^{41}\ n_e^2\ \zeta\ f_v\ V_{\mathrm{kpc}} \quad \mathrm{erg\,s^{-1}} \tag{1}$$

(Osterbrock 1989). Here n_e is the electron density in $\mathrm{cm^{-3}}$, ζ is the oxygen abundance relative to the solar value, f_v is the volume filling factor of the line emitting gas, and V_{kpc} is its volume in $\mathrm{kpc^3}$. Assigning a value to the degree of 'clumpiness' of the gas is the greatest uncertainty in determining the overall density, with filling factors ranging from 3×10^{-4}, as measured from [SII] line ratios in low redshift radio galaxies (Heckman et al. 1984), to 2×10^{-6} for line-emitting gas associated with cooling flows (Heckman et al. 1989). Taking a volume of $5.1 \times 10^4\,\mathrm{kpc^3}$, a filling factor midway between the observed extremes (10^{-5}), and a relative oxygen abundance of 0.03, gives an average density of the [O II]$\lambda 3727$ gas of $n_e \sim 130$ $\mathrm{cm^{-3}}$. If we assume that the gas in

3C 34 is completely ionized, the average density and volume computed above give a total mass of warm gas in 3C 34 of $M_{gas} \sim 2 \times 10^9$ $M_\odot$.

3.1.2. Optical Continuum Morphology

3C 34 is equally spectacular in the light of our deep line-free continuum image. This galaxy appears to lie in a rich, compact cluster, with 18 possible companion galaxies within a radius of 200 kpc of the central source (see figures 1 and 2). With the exception of component A, however, we do not detect [O II]λ3727 line-emission from any other continuum source in the field despite a Fabry-Perot velocity coverage of -1600 km s$^{-1} \leq \Delta v_\circ \leq +1300$ km s^{-1}, in the rest frame of the central galaxy. In fact, the many continuum sources surrounding the central radio galaxy appear to avoid the contours associated with the line-emission image.

Near to the center of the cluster lies the brightest source, component A. This galaxy is positioned almost exactly at the center of the radio emission and is identified as the optical counterpart to the radio source (Riley et al. 1980). From the line-emission associated with component A we compute a redshift for this central source of z=0.6900 ± 0.0007. As is evident from figure 3, the core of component A is only marginally different from a stellar profile. However, beyond a radius of about $2''$ A appears to be embedded in a broad continuum halo, within which a number of faint knots of emission can be seen. The central continuum component A, as derived from our continuum frame and 17 reference stars from the PPM catalogue (Röser & Bastian 1991), has an absolute position of

$$\alpha = 01^{\mathrm{h}} \ 07^{\mathrm{m}} \ 32\overset{\mathrm{s}}{.}55 \qquad \delta = +31° \ 31' \ 22\overset{''}{.}8 \qquad (1950.0),$$

with an uncertainty of $\pm 0\overset{''}{.}5$ in both coordinates. This position was used to place the radio contours in figure 2 and agrees to within $0\overset{''}{.}6$ of the radio nucleus detected in the λ6 cm and λ20 cm observations of Johnson et al. 1995.

To the north of the radio galaxy lies a close (at least in projection) companion galaxy, component C. Although this companion is close enough to component A to share its outer halo emission at the lower flux levels, it is undoubtably a distinct source. Inspection of the line-emission images at the faintest flux levels and at all wavelengths, revealed no [O II]λ3727 counterpart to this continuum source. Therefore, we cannot assign a redshift to this component.

In contrast to the line-emission image, the crowded continuum environment of 3C 34 makes an unequivocal determination of the position angle of the host galaxy difficult. Beyond a radius of $\sim 3''$ from the central radio galaxy the position angle changes sharply, as a number of companion sources, in particular component C, enters the aperture. However, since the companion source C is distinct from the radio galaxy at the brighter flux levels with no associated [O II]λ3727 detection, we determined a position angle that is confined to the direct environment of component A. Within an aperture of $3\overset{''}{.}0$ radius centered on this source, with component C subtracted from the image,

the continuum position angle was found to be $106° \pm 5°$. Thus the continuum emission is well aligned with the line-emission (ΔPA(|line–continuum|)=3°) and only moderately aligned with the radio source (ΔPA(|radio–continuum|)=21°).

In table 1 we present a synopsis of the relative positions, physical separations, continuum magnitudes, [O II]λ3727 flux levels, and FWHM of the continuum and line-emission components observed in 3C 34.

3.2. Kinematics: Radial Velocities and Deconvolved Line Widths

Figure 4 illustrates line profiles at specific positions in the line-emission region of 3C 34. The velocity map obtained from the fit to the Fabry-Perot data cube is shown in figure 5, with the velocity and FWHM profiles along the three major regions of 3C 34 shown in figure 6. The kinematical and positional origins of figures 5 and 6 are defined by the radio galaxy center. Compared to the other sources in our overall sample the range of velocity spanned by 3C 34, in particular considering the extreme size of its emission-line region, is quite moderate. The dynamical structures visible in this source, based on their shape and absolute velocity, can be divided into the same three distinct regions that were used in describing the line-emission morphology. The velocity of the [O II] gas in the central region of 3C 34 (figure 6 central panel) is distinguished by a relatively smooth velocity bump spanning $0\,\mathrm{km\,s^{-1}}$ near the center of this region, to -500 $\mathrm{km\,s^{-1}}$ at its northeast and southwestern ends. The line-emission sources A and B are positioned on either side of this feature. The corresponding line widths show an obvious minimum at the position of this velocity peak, which is $\sim 1''$ to the northeast of component A. This local FWHM minimum is at $300\,\mathrm{km\,s^{-1}}$ and rises steadily away from both A and B to $\sim 750\,\mathrm{km\,s^{-1}}$ and $550\,\mathrm{km\,s^{-1}}$ respectively. The subsequent decline in the FWHM observed in figure 6, beyond about -3$''$ and +2$''$, may be due to low flux levels resulting in poor fits to the data cube, or to a slight over-subtraction of the continuum.

The eastern region of 3C 34 is surprisingly flat at velocity values near $-400\,\mathrm{km\,s^{-1}}$. The fact that the deviations from this velocity value are always less than about $150\,\mathrm{km\,s^{-1}}$ is remarkable considering that this side of the source spans more than $70\,\mathrm{kpc}$ of projected line-emission. The associated velocity widths of this region reveal a number of low significance undulations. The FWHM on this side of the 3C 34 are the lowest for the entire source and, in an absolute sense, the average FWHM ($\lesssim 250\,\mathrm{km\,s^{-1}}$) of this region is remarkably quiescent.

To the west of 3C 34 we observe a very sudden velocity change in going from the gradual decline still visible from the central region, out to component a. This velocity discontinuity spans about $690\,\mathrm{km\,s^{-1}}$ from the western end of the central region to the beginning of source a. This is most evident in our two-dimensional velocity images (figure 5) and points to the fact that we are seeing an overlap of two distinct sources (*i.e.* component A and component a). This superposition of sources results in the large FWHM seen at this position. At the location of component a, we

see the maximum overall velocity for 3C 34 (v=500 km s^{-1}). Across the remainder of the western region the velocity remains relatively flat.

4. Discussion

4.1. Photoionization by a Hidden AGN

Most noteworthy about the morphology of 3C 34 is that the line-emission exhibits a bi-conical shape with the nucleus of this radio galaxy at the apex of the cones. We will argue that this unique shape is the result of an ambient medium swept aside by the radio source, and subsequently illuminated by a collimated source of ionizing radiation.

Since the likeliest location of the active nucleus lies at the centroid of continuum component A, we will designate this as the origin of the cone. We will also assume the photoionization cone to be close to the plane of the sky; an assumption consistent with the narrow gap between the radio lobes and the evidence for jets on both sides of the source (Johnson et al. 1995). As is shown in figure 7, it then immediately follows that a straight line can be drawn from the peak of component c, through the origin, to the peak of the finger of emission northwest of component a. Similarly, a straight line can be drawn through component B, the origin, the line-emission component A, and the center of the faint extension of line-emission at the southwestern end of component A. Thus, simply by placing the apex of a symmetrical bi-cone at the position of the central continuum source, we find that we can connect 6 distinct line-emission knots/extensions on both sides of 3C 34 and symmetrically straddle the radio source axis. Drawn in this way, the bi-cone has an opening angle of 60°. However, since it is defined by the positions of the peak intensities of the brightest emission-line components, the true opening angle necessary to photoionize all of the [O II] gas may be somewhat larger. A bi-cone drawn through the same center, but using the outer FWHM positions of components B and c, results in an opening angle of about 90°.

Such a conical structure in 3C 34, though unobserved in high redshift radio galaxies, has been observed in low redshift Seyfert galaxies and in 3C 227 (z=0.085) (Prieto et al. 1993). Currently 11 such Seyferts are known to possess an ionization cone or a bi-cone—8 of which also contain a linear radio structure (*i.e.* a double, triple, or jet-like radio source) (Wilson & Tsvetanov 1994). From these sources Wilson & Tsvetanov 1994 find that there is a tight alignment between the cone and radio axes, with a mean difference in position angle of only 6°, and that the degree of collimation is much better for the radio plasma than for the ionizing photons. This is exactly what is observed in 3C 34. As in the Seyferts, the bi-cone of 3C 34 is situated almost exactly along the axis defined by the radio emission, with ΔPA = 4°. The prominent cones in Seyferts and 3C 227, however, show emission across the entire lateral extent of their opening angles (see, for example, the [O III]λ5007 image of NGC 5252 in Tadhunter & Tsvetanov 1989). This is not true for 3C 34, where the line-emitting gas appears to be confined to the outer edges of the ionization cone and by no means fills it.

Aside from explaining the overall conical morphology of 3C 34, the photoionization model can be applied to a number of smaller-scale features seen in line-emission. The intensity profiles of components c and a on the eastern and western side of the bi-cone, respectively, are both markedly steepened on their sides facing the central source (see figure 3). This could be due to geometrical dilution or by absorption or scattering in intervening material closest to the central source. It is also possible that radiative bounding of the ionizing flux from the central galaxy can give rise to the morphology seen in source B, and in the western component. The steep fall-off in intensity and the lack of any line-emission outward from component B points toward this source being a very dense knot of gas capable of absorbing all of the incident ionizing radiation. It is also plausible that component a is 'shadowing' the ionizing emission from the AGN, and preventing this flux from reaching the gas to its immediate west. The small lateral extent of source a may allow the ionizing radiation to reach the gas surrounding it to the north and south, causing the two fingers of [O II] emission observed extending to either side of component a. The ionizing radiation reaching the gas on the western side of 3C 34 could be somewhat diluted due to strong absorption occurring in the central component A. This would, in turn, allow component a to effectively absorb the remaining radiation and at the same time remain relatively faint. An alternative explanation for the fall-off in [O II] emission outward from components B and a could, of course, be a simple paucity of gas beyond these sources.

A critical test of our photoionization model is whether or not the central, hidden AGN can provide enough ionizing photons to excite the [O II] emitting gas observed in 3C 34. The two best line-emission sources on which to test this are component c, because it is furthest from the central galaxy, and component B, because it is the brightest source beyond the central galaxy. The very sharp fall-off in [O II] brightness on the side of component B facing away from the central source, argues for a region that is radiation bounded. Furthermore, since the [O II] flux integrated across the eastern component out to source c is almost identical to that observed for source B, we will assume that c is also radiation bound. Thus, a covering factor of unity will be used for these two sources.

A description of the model that we have used to estimate the luminosity of the central source, necessary to photoionize the observed line-emission regions, is given in the appendix. This model assumes that the central ionizing source has a spectral index of 1.0 and that the ratio of ionizing photons to resulting [O II]$\lambda3727$ photons is 6:1. Then, using equation A6 we have computed the required luminosity of the central source necessary to produce the [O II]$\lambda3727$ flux observed in components B and c. The results of this computation are summarized in table 2 using source radii based on both the FWHM and the total lateral extent of components B and c, and two different ionization cone opening angles. Clearly, component c is the most critical source due to its distance from the central galaxy. Even with the worst case parameters of a large 88° opening angle and a small radius, we conclude that the required luminosity of the hidden, photoionizing AGN is reasonable, at roughly a factor of three lower than the B-band luminosity of the brightest 3C quasar. If viewed along a line-of-sight down the ionization cone the apparent V-band magnitude

(see column 6 of table 2), assuming zero extinction, would be comparable to a typical 3C quasar at the redshift of 3C 34 (Allington-Smith 1984).

Of course, the evidence for photoionization in 3C 34 could be improved using line ratio diagnostics. For such tests a number of low-to-high ionization lines would have to be detected in the faint, extended line-emission region (*e.g.* component *c*). The literature shows, however, that even the detection of a sufficient number of lines in the considerably brighter nucleus has been difficult; the high ionization lines [Ne III]λ3869 and [Ne IV]λ3426 were found to be very weak and undetectable, respectively, in the spectrum of Spinrad et al. 1985, and Rawlings et al. 1991 failed to detect the [S III]λ9532 line in their near-infrared spectrum.

4.2.   The [O II] Kinematics and Radio Source Expansion/Backflow

The final issue that must be addressed is how the velocities observed in the [O II] gas of 3C 34 fit into the photoionization framework. The simplest model would assume that the ionization cone is merely illuminating gas clumps, of random velocity, that exist in a typical cluster environment. The abrupt velocity discontinuities between the central source and the two line-emission regions to the east and west would tend to support such a picture. The overall velocity spanned by the entire line-emission region is also consistent with a rich cluster (*e.g.* Dressler & Gunn 1992). The difficulties with this interpretation, however, arise when one considers that the [O II] line-emission in 3C 34 is uninterrupted across more than 140 kpc—unusual considering that the warm gas in a cluster environment is usually considered to be in discrete clumps or filaments unconnected over such large regions. Even more fatal to the cluster interpretation is the fact that the eastern component shows a remarkably flat velocity structure across a length of more than 70 kpc. Such uniformity across such large distances is incompatible with the essentially random velocity dispersions associated with clusters. In fact, the constant velocity across the entire eastern line-emission region would seem to indicate that a *single* mechanism is required to act on a large fraction of gas simultaneously.

As is clear from figure 2 the eastern line-emission region is near the outer edge of the radio source, and also seems to conform well to the radio contours. We therefore propose that the radio source has, through the bulk motions of its lateral expansion, enmasse swept up the gas that existed in the environment of 3C 34. In this way the gas that makes up the eastern [O II] line-emission region is compressed, pushed to the outer edge of the radio, and given a bulk velocity that is constant across the entire region. The connection between the radio lobes and the line-emission gas is corroborated by the orientation of 3C 34, independently deduced from the radio observations and our optical data.

Radio polarization measurements of 3C 34 by Johnson et al. 1995, find a higher degree of depolarization in the eastern radio lobe, particularly prominent along the position of the line-emitting gas. The western side of 3C 34, on the other hand, shows no similar match between

the location of its line-emission gas and depolarization in the radio lobe. This supports our radio lobe expansion and backflow interpretation of the blue– and redshift observed in the eastern and western line-emission regions; namely, that the line-emission to the east of 3C 34 is oriented toward us, while the western region points into the plane of the sky.

Lateral expansion in the radio source lobes may also be playing a significant role in defining the velocity observed in the western line-emission region. In this case its redshifted velocity with respect to the central galaxy could be due to the far side of the radio lobe expanding away from us and sweeping the gas along with it. The fact that the western line-emission region is symmetrical with respect to the radio axis may be due to the gas spreading both north and south as the far side of the radio lobe sheath expands. Alternatively, the western line-emission region, as is indicated by the velocity and line width discontinuity between this region and the central source, may simply be a distinct gas cloud that is being illuminated by the ionization cone of 3C 34. We are currently unable to distinguish between these two interpretations.

More difficult to explain is the velocity structure observed in the central line-emission region. The smooth velocity bump may indicate some form of mass inflow or outflow, whose asymmetry may be intrinsic, or due to some form of extinction that inhibits our view of the far-side velocity surface. Alternatively, if we assume that the radio lobes lie behind both the northeast and southwest ends of this component, but do not extend all the way to the center of the source (as seems to be indicated in figure 2), backflow and/or cocoon expansion could selectively push these ends toward our line-of-sight and create the observed velocity bump. Radio source backflow is indicated by the prominent 'wings' of radio emission near to the central source, that extend perpendicular to the major axis (see figure 2). The close correspondence between the radio source and the NE end of component B, as well as the velocity width maxima observed at the ends of both central components (see figure 5), could be the result of such an interaction. It is interesting to note that the NE line width maximum is not symmetric with respect to the major axis of the central component $(A + B)$, but lies along the radio source axis.

In our photoionization scenario there exists a direct cause and effect relationship between the radio ejecta and the ionization cone that leads to their alignment. It is possible to imagine that the nucleus was initially surrounded by a cloud opaque to ionizing radiation in all directions. When the radio jet turned on it plowed through the cloud and opened up a low density channel. As the radio lobes grew in size the increased density of the swept up gas at its outer edges allows it to effectively absorb the incident ionizing radiation from the central AGN which, in turn, can effectively escape along the cleared out, low density channel created by the radio source. If this is indeed the case, one might expect that the line-emitting gas would be edge-brightened on its radio source side due to the enhanced density along this interface. The intensity contours of our [O II]λ3727 map show the exact opposite; the eastern line-emission region has a higher surface brightness on the side facing away from the central axis of the radio source. If we assume that the gas of the eastern line-emission region wraps slightly around the bottom surface of a cylindrically shaped radio lobe (an interpretation consistent with the depolarization at this position), then the

brightening we perceive at the outer edge of the [O II] emission could be due to foreshortening. Instead of looking at a thin sheath of gas, as along the northern side of this line-emission region, we see a slightly greater column depth of gas at the bottom edge of this feature (see figure 8).

The evidence for directed radiation from a hidden nucleus provides supporting evidence for the 'unified models', that attempt to explain the relationships between active galaxies and quasars in terms of anisotropic emission and orientation effects (*e.g.* Barthel 1989; Antonucci 1993). The high redshift and very extended line-emission of 3C 34 makes this source an important example for this class of object. In light of this, it is important to ask the question why the morphology of the line-emission gas observed in 3C 34 is so different from the ionization cone-filling morphology common in Seyfert galaxies. The answer to this is twofold. First, we will use NGC 5252 (cz=6852 km s^{-1}) as a suitable comparison; it represents a well defined example of photoionization in Seyferts, and has the largest known ionization cone with a total extent of roughly 36 kpc. In our image of 3C 34 this would correspond to the first 2″.3 on either side of the source and hence be well within the line-emission surrounding components A and B. At this inner position it may well be that the line-emitting gas fills the lateral extent of the ionization cone. Spatial resolutions better than $\sim$0″.4 FWHM would be necessary to adequately resolve the warm gas this near to the central galaxy. An alternative explanation, however, along the lines of the 'unified models', would be that the ionization cones in both NGC 5252 and 3C 34 began in similar environments with both initial radio sources clearing out channels in the gas that eventually allowed the photoionizing radiation to escape. However, whereas the radio source in NGC 5252 has $P_{6cm} = 3.4 \times 10^{28}$ erg s^{-1}Hz^{-1}sr^{-1} and is very modest in size (Tadhunter & Tsvetanov 1989), 3C 34 is more than 10^4 more powerful at this wavelength. It is therefore plausible that only the considerably more powerful radio source in 3C 34 (and high redshift FR II radio galaxies in general) is capable of effectively sweeping out the IGM of its host source and confining the line-emission gas to its edges.

4.3. Alternative Interpretations

The ability of our photoionization model, in combination with radio source backflow and expansion, to explain the observed line-emission morphology and kinematics, does not guarantee that it is the only possible interpretation of 3C 34. We therefore feel obliged to account for possible alternative models, and discuss why we consider them to be inferior to our model in explaining our observational results.

4.3.1. Radio Source Collisional Excitation

The fact that the line-emission gas in 3C 34 extends great distances on either side of the central radio galaxy, the average overall alignment between the [O II] emitting gas and the radio source, and the general red-to-blueshift velocity trend across the source, would seem to point to

a direct collisional interaction between these two media. A closer look at a number of detailed features, however, can rule out this scenario as the main mechanism for ionizing the [O II] gas.

Although there does exists an overall red-to-blueshift trend in going from west to east in 3C 34, the velocity changes are abrupt and then remain almost constant across the length of the eastern line-emission region. Along the entire 70 kpc of this [O II] region the total velocity variation is less than $150 \, \mathrm{km \, s^{-1}}$ and is associated with moderate line widths of only about $250 \, \mathrm{km \, s^{-1}}$. This gives 3C 34 a velocity profile and line widths unlike those observed in powerful radio galaxies in which jet–cloud interactions are more obviously involved in creating the observed emission-line regions. At low redshifts examples of such sources include 4C 29.30, 3C 171, and PKS 2250–41 (van Breugel et al. 1986; Heckman et al. 1984; Clark & Tadhunter 1996), while for high redshifts 3C 352 and 3C 368 (Meisenheimer & Hippelein 1992; Hippelein & Meisenheimer 1992) are obvious candidates. In all of these sources the dynamical effect of the radio jet on the line-emitting gas is considerable with major axis velocity gradients of up to $1000 \, \mathrm{km \, s^{-1}}$ and line widths $\gtrsim$ $1000 \, \mathrm{km \, s^{-1}}$. A further characteristic of these radio source—ambient medium interaction objects is the relatively close correlation between the radio and line-emission morphologies. In 3C 34 this is obviously not the case, with the size of the radio source exceeding the regions of [O II] emission by more than a factor of two.

A critical test of a direct interaction between the radio source working surface and the gas that it excites and compresses are the implied cooling times. Assuming an angle between the line-of-sight and the radio source axis of 75° (Johnson et al. 1995), the deprojected flow velocity near component c would be $370 \, \mathrm{km \, s^{-1}} \times \cos^{-1}(75°) \simeq 1400 \, \mathrm{km \, s^{-1}}$. By relating the shock temperature to the temperature of the ambient external medium and the mach number of their highly supersonic model, Meisenheimer & Hippelein 1992 deduce an expression that relates the advance speed of the radio source bow shock (V_{bow}) to the temperature of the shock (T_{sh}),

$$V_{bow} = 0.28 \ T_{\mathrm{sh}}^{1/2} \quad \mathrm{km \, s^{-1}}. \tag{2}$$

Using this relationship we estimate that such a shock will heat the gas in 3C 34 to $T_{\mathrm{sh}} \sim 2.5 \times 10^7 \, \mathrm{K}$. In terms of this temperature immediately behind the bow shock and the density n_c in the shocked gas clouds, the cooling time is given by

$$\tau_{\mathrm{cool}} = \frac{E}{|dE/dt|} \simeq 1.27 \, \frac{T_{\mathrm{sh}}}{n_c} \quad \mathrm{years}. \tag{3}$$

For the low metallicities expected for the IGM around high redshift radio galaxies and shock temperatures $\gtrsim 10^7 \, \mathrm{K}$, we have assumed a constant cooling coefficient $\Lambda(T) \simeq 10^{-23} \, \mathrm{erg \, cm^3 \, s^{-1}}$ (Böhringer & Hensler 1989). Using a canonical ambient medium post-shock density of $n_c \sim 1 - 10 \, \mathrm{cm^{-3}}$ along with the derived shock temperature in equation 3, we can then compute the time required for the shocked plasma to cool to about $2 \times 10^4 \, \mathrm{K}$. We find that $\tau_{\mathrm{cool}} \sim 3 \times 10^7 - 3 \times 10^6$ years are needed before this region can emit in its [O II]λ3727 line. The dynamical age of the interaction, however, as derived from the estimated shock velocity and the distance between component c and the radio source hotspot ($d \simeq 150 \, \mathrm{kpc}$), is on the order of 1×10^8 years. Thus,

with $\tau_{\rm dyn}/\tau_{\rm cool} \gtrsim 3 - 30$ for the eastern emission-line component the gas would have since cooled, and with the short radiative lifetime of its current line-emission luminosity (see below), cannot now be radiating the energy given to it by the radio source bow shock.

Of course, an alternative to a one-time energy injection could consist of secondary shocks driven into the cocoon surrounding the supersonic jet itself, or a more recent input of energy via the lateral expansion of the radio lobes. Although we cannot entirely discount such models, and it is certainly possible that some fraction of the excitation of the eastern line-emission region is due to collisional excitation by the radio lobe, the extremely quiescent velocity widths and large luminosity in this [O II] gas, are difficult to explain solely with this interpretation. For example, by assuming that the velocity dispersion of the [O II]$\lambda 3727$ gas is representative of the material that constitutes the bulk of the ionized gas mass, the total kinetic energy of this medium will be of the order

$$E_k = 1 \times 10^{55} \ M_8 \ \sigma_{100}^2 \quad \text{erg}, \tag{4}$$

where M_8 is the mass of the ionized gas in the eastern region in units of 10^8 M$_\odot$, and σ_{100} is the total velocity dispersion in units of $100 \, {\rm km \, s^{-1}}$. For the eastern line-emission region we find $M_{\rm gas} = 3.4 \times 10^8$. If we further assume that the observed radial line widths in this region are solely the result of turbulent motions in an isotropic system, $\sigma = \sqrt{3} \cdot 130 \, {\rm km \, s^{-1}}$. This means that the kinetic energy of the warm ionized gas is of the order of 2×10^{56} erg. Given the total luminosity of this region one derives a radiative lifetime of the line-emission gas of

$$\tau = 3 \times 10^4 \ \frac{E_{k\,56}}{L_{\rm lines\,44}} \ \epsilon \quad \text{years}, \tag{5}$$

where $E_{k\,56}$ is the kinetic energy in units of 10^{56} erg, $L_{\rm lines\,44}$ the luminosity of all the emission-lines in units of $10^{44} \, {\rm erg \, s^{-1}}$, and ϵ the efficiency factor in converting turbulence to line-emission. So, with conversion efficiencies ranging from 1 to 100% the dissipation time of the shock excited gas is only 140 to 1.4×10^4 years.

4.3.2. Photoionization by a Jet-Induced Starburst

Since most high redshift radio galaxies have blue colours, perhaps indicative of large scale bursts of star formation, it has been suggested that the direct interaction between the outflow along the radio source axis and the IGM is the trigger for this phenomena (*e.g.* McCarthy et al. 1987 and Chambers et al. 1987). Although it is not a general phenomena, there is evidence that jet-induced star formation does indeed occur in low redshift sources such as Minkowski's object (van Breugel et al. 1985). Aside from providing a natural explanation for the radio/optical alignments, this model also provides a means of delivering ionizing radiation directly to the line-emitting gas. Therefore, the large extent of its line-emission region and its relatively close alignment to the radio axis makes 3C 34 a possible candidate for the jet-induced starburst scenario.

To see whether this model is compatible with our observations, we will use the spectral evolution models of Bruzual & Charlot 1993 to test whether the OB stars, produced by the passage of the radio source working surface, can provide a sufficient number of ionizing photons to *in situ* excite the surrounding line-emitting regions. For simplicity we have chosen an instantaneous burst model with a Salpeter initial mass function (IMF) (Salpeter 1955) that is weighted toward the high stellar mass end such that $2.5 \leq M \leq 125\ M_\odot$. Though extreme by comparison to other available models, the choice of an instantaneous starburst is made in order to provide the greatest amount of UV photons per stellar mass involved. The same is true for the choice of IMF and stellar mass range. Furthermore, the short duration of the radio source phenomena forces the need to convert the gas, shocked and compressed by the radio jet or its pressure cocoon, into stars in the shortest time possible. A maximum number of ionizing photons in the galaxy rest frame are created by this model at a time $\tau \sim 3.3 \times 10^6$ years after the initial burst. By integrating the resultant starburst spectrum blueward of the Lyα line we find that 5.1×10^{47} photons s^{-1} M$_\odot{}^{-1}$ are available to photoionize the ambient gaseous medium per solar mass of the starburst.

The [O II]$\lambda 3727$ luminosities observed in the line-emission components B, a, b, and c, the likeliest sites for the location of an underlying starburst, can then be divided by this number to determine the minimum total mass of the starburst necessary to produce the required ionization. The computed masses range from 7×10^6 M$_\odot$ for component b, to 3×10^7 M$_\odot$ for source B. Barring extinction effects in the environment of the radio galaxy, which would undoubtably also affect the observed line-emission, these masses can be converted to observed flux levels by integrating the starburst spectrum over our the wavelength range sampled by our continuum filter ($\lambda_\circ$=4033Å ($\Delta\lambda_\circ$=107Å)). The resulting flux values have been converted to counts in this filter and added to our continuum image of 3C 34. Figure 9 shows these model starbursts to be very obvious at the positions of components B and c. (The more subtle enhancements at the positions of a and b are due to the weaker line-emission and pre-existing continuum at these positions). The absence of such obvious starburst continuum signatures in the original image (see figure 1b), near sources B and c, strongly excludes this model for the ionization of the line-emission regions in 3C 34.

5.   Summary and Conclusions

Our morphological and kinematical study of 3C 34 favours a scenario in which the extended emission-line region is excited by the photoionizing UV radiation emitted by the central, hidden AGN. This model goes far in explaining the overall conical morphology of 3C 34's warm gas, and the detailed shapes of its individual [O II] knots. Furthermore, the energy budget necessary to excite this extended gas remains compatible with the central luminosity of typical 3C quasars at the same redshift. To account for the observed line-emission kinematics, however, requires an additional weak interaction between the radio lobes and the ambient medium. The large, quiescent, blueshifted velocity structure across the entire eastern region of 3C 34, as well as the redshifted velocity discontinuity of the western region, are best explained as gas swept aside by

the lateral expansion of the radio cocoon. This is corroborated by the spatial coincidence between the edges of the radio lobes and the [O II] gas, and by the radio depolarization at positions where this gas is in direct contact with the radio lobes. In this model the alignment of the [O II] region with the radio source arises from both emission signatures originating from the same central engine, and by the fact that the ionizing radiation preferentially escapes along an axis in which the ambient medium has been cleared by the radio source. The identification of 3C 34 with a cone of photoionization may be the first detection of such a feature in a high redshift, powerful radio galaxy. As such, this source can be an important link to the low redshift, low luminosity Seyfert galaxies in which such photoionization cones have traditionally been observed.

It should be noted that the line-emission morphology and kinematics of 3C 34 are unique in our current [O II] sample of 11 radio galaxies. This means that we cannot claim photoionization by a hidden, central AGN to be a general mechanism for exciting the line-emission regions observed in all powerful radio galaxies. In fact, at least two further means of ionization are necessary to explain the line-emission morphology and kinematics of all the sources in our sample: shock excitation of the ambient gaseous medium by an interaction with the radio source (Meisenheimer & Hippelein 1992; Hippelein & Meisenheimer 1992), and strong galaxy–galaxy interactions (Neeser et al. 1997). This argues against any universal, all-encompassing model for the alignment effect in powerful radio galaxies; a fact also supported by the need for both photoionization and radio source expansion and backflow to explain most aspects of 3C 34's line-emission regions.

A. Photoionization by a Hidden AGN

A critical feature of a photoionization model is that the central AGN be able to provide a sufficient number of ionizing photons, to satisfy the total luminosity observed from the line-emission regions it is supposedly exciting. The number of ionizing photons emitted by the hidden AGN into a cone of solid angle, Ω_{beam}, and intercepted by a cloud at a distance R from the central source is,

$$\mathcal{N}_{\text{ion}}(\nu) = \frac{A}{\Omega_{\text{beam}}R^2} \int_{\nu_c}^{\infty} \frac{L_{\text{ion}}(\nu)}{h\nu} \, d\nu. \tag{A1}$$

Here, $L_{\text{ion}}(\nu)$ is the ionizing luminosity emitted by the AGN, A is the effective area of the cloud as seen from the AGN, and the integration is over all frequencies above the Lyman-continuum (ν_c). We assume that the ionizing radiation emitted by the central AGN obeys a non-thermal power-law of the form

$$L_{\text{ion}}(\nu) = C\nu^{-\alpha} \qquad (\alpha > 0), \tag{A2}$$

where C is a constant and α is the spectral index of the far–UV energy distribution of the central source. Equation A2 can then be substituted into equation A1 and integrated such that,

$$\mathcal{N}_{\text{ion}} = \frac{AC\nu_c^{-\alpha}}{\Omega_{\text{beam}}R^2h\alpha}. \tag{A3}$$

This number of 'expected' ionizing photons must then be compared with the 'observed' number of [O II]λ3727 photons emitted by the cloud, $\mathcal{N}_{\text{[OII]}}$. However, to relate the incident radiation to the observed [O II]λ3727 line-emission we must take into account the ratio, k, of the number of ionizing photons required to produce one observed [O II]λ3727 photon. Furthermore, the effectiveness with which a given clump of gas absorbs incident photons is critically dependent on the covering factor, f_c — the fraction of the sky, as seen by the nucleus, covered by optically thick clouds. Combining these two factors we can then compute the effective number of ionizing photons impinging on the cloud, in terms of the observed number of [O II]λ3727 photons emitted by the cloud,

$$\mathcal{N}_{\text{eff}} = \frac{k}{f_c} \frac{L_{\text{[OII]}}}{h\nu_{\text{[OII]}}}. \tag{A4}$$

Comparing equations A4 and A3 and solving for the constant C, which is then introduced into equation A2 gives the monochromatic luminosity that the hidden AGN must emit to produce the observed line-luminosity,

$$L_{\text{ion}}(\nu) = \frac{k}{f_c} \frac{L_{\text{[OII]}}}{h\nu_{\text{[OII]}}} \frac{\Omega_{\text{beam}}R^2h\alpha}{A} \left(\frac{\nu}{\nu_c}\right)^{-\alpha}. \tag{A5}$$

Most critical for this photoionization model will be those emission-line components that have the highest surface brightness and lie furthest from the central source. But, before this equation can be applied to these sources a number of further assumptions must be made about the variables in this expression. For simplicity, we will assume that the projected area of the [O II]

sources (clouds) is similar to the actual total area facing towards the continuum source, with a circular cross-section having a characteristic radius (r) of one-half the knot's FWHM. We must also consider what fraction of the ionizing radiation goes into producing the observed [O II]λ3727 flux. Assume that the environment of our radio galaxies can be approximated by the radiative transfer properties in a giant extragalactic HII region, we can use the model results of Stasinska 1980. Using parameters typical of the line-emission gas observed in our sources; a temperature of $T_{\rm eff}$=4.5 × 10^4, a metal abundance relative to solar of $Z/Z_\odot \lesssim$0.2, and interpolating between the computed densities $10 < {\rm n}_e < 100$ cm^{-3}, this model gives an [O II]λ3727 to $H\beta$ ratio of 1.5. For case B recombination, the ratio of the number of $Ly\alpha$ to $H\beta$ photons is 8.5 (Osterbrock 1989). Therefore, we estimate that the number of photoionizing photons required for every [O II]λ3727 photon produced is $k \sim$6. Finally, we will assume a spectral index of $\alpha = 1$ (Villar-Martin et al. 1997).

With these assumptions in place, equation A5 can be used to compute the *required* luminosity that the ionizing source must have in order to produce the observed [O II]λ3727 flux. By integrating this expression with respect to ν, over any filter of interest that covers a rest frame wavelength range of $\lambda_1 < \lambda < \lambda_2$, we can determine the broad–band luminosities the AGN must produce. In this way the required luminosity can be simplified to contain only those parameters specific to an individual source,

$$L_{\rm ion}^{\lambda} = 24.5 \ L_{\rm [OII]} \ \frac{\Omega_{\rm beam} R^2}{f_c A} \ ln\left(\frac{\lambda_2}{\lambda_1}\right) \quad {\rm erg \, s}^{-1}. \tag{A6}$$

This, in turn, can be converted to expected apparent magnitudes if the ionizing beam from the hidden ionizing source were directed toward us. The resulting luminosity and magnitude can then be compared with values from known 3CR quasars at redshifts similar to that of 3C 34. Since the 'unifying schemes' assume radio galaxies to differ from quasars primarily in terms of orientation, the luminosity that we compute to be necessary to photoionize the observed line-emission, must be less than or equal to those observed for the intrinsically brightest quasars.

REFERENCES

Allington-Smith, J. R. 1984, MNRAS, 209, 665

Antonucci, R. 1993, Ann. Rev. Astron. Astrophys., 31, 473

Barthel, P. D. 1989, ApJ, 336, 606

Böhringer, H., & Hensler, G. 1989, A&A, 215, 147

Bruzual, G. A., & Charlot, S. 1993, ApJ, 405, 538

Burstein, D., & Heiles, C. 1982, AJ, 87, 1165

Chambers, K. C., Miley, G. K., & van Breugel, W. 1987, Nature, 329, 604

Clark, N. E., & Tadhunter, C. N. 1996, Cygnus A – Study of a Radio Galaxy, ed. C. L. Carilli & D. E. Harris, Cambridge University Press, 15

Dressler, A., & Gunn, J. 1992, ApJS, 78, 1

Garrington, S. T., Conway, R. G., & Leahy, J. P. 1991, MNRAS, 250, 171

Heckman, T. M., Baum, S. A., van Breugel, W. J. M., & McCarthy, P. J. 1989, ApJ, 338, 48

Heckman, T. M., van Breugel, W. J. M., & Miley, G. K. 1984, ApJ, 286, 509

Hippelein, H., & Meisenheimer, K. 1992, A&A, 264, 472

Jenkins, C. J., Pooley, G. G., & Riley, J. M. 1977, Mem. R. Astron. Soc., 84, 61

Johnson, R. A., Leahy, J. P., & Garrington, S. T. 1995, MNRAS, 273, 877

McCarthy, P. J., van Breugel, W., Spinrad, H., & Djorgovski, S. 1987, ApJ, 321, L29

McCarthy, P. J., Spinrad, H., & van Breugel, W. 1995, ApJS, 99, 27

McCarthy, P. J., Baum, S. A., & Spinrad, H. 1996, ApJS, 106, 281

Meisenheimer, K., & Hippelein, H. 1992, A&A, 264, 455

Neeser, M. J., Hippelein, H., & Meisenheimer, K. 1997, in prep

Neff, S. G., Roberts, L., & Hutchings, J. B. 1995, ApJS, 99, 349

Osterbrock, D. E. 1989, *Astrophysics of Gaseous Nebulae & Active Galactic Nuclei*, University Science Books

Prieto, M. A., Walsh, J. R., Fosbury, R. A. E., & di Serego Alighieri, S. 1993, MNRAS, 263, 10

Rawlings, S., Eales, S., & Lacy, M. 1991, MNRAS, 251, 17P

Riley, J. M., Longair, M. S., & Gunn, J. E. 1980, MNRAS, 192, 233

Röser, S., & Bastian, U. 1991, PPM Star Catalogue, Spektrum, Akademischer Verlag, Heidelberg.

Salpeter, E. E. 1955, ApJ, 121, 161

Spinrad, H. 1982 PASP, 94, 397

Spinrad, H., Djorgovski, S., Marr, J., & Aguilar, L. 1985 PASP, 97, 932

Stasinska, G. 1980, A&A, 84, 320

Tadhunter, C. N., & Tsvetanov, Z. I. 1989, Nature, 341, 422

van Breugel, W. J. M., Filippenko, A. V., Heckman, T. M., & Miley, G. K. 1985, ApJ, 293, 83

van Breugel, W. J. M., Heckman, T. M., Miley, G. K., & Filippenko, A. V. 1986, ApJ, 311, 58

Villar-Martin, M., Tadhunter, C., & Clark, N. 1997, A&A, in press

Wilson, A. S., & Tsvetanov, Z. I. 1994, AJ, 107, 1227

Fig. 1.— Labelled components of 3C 34 as discussed in text. (a) Continuum subtracted [O II]λ3727 image. (b) Line-free continuum image with a rest-frame wavelength of $\lambda_\circ$=4033Å ($\Delta\lambda_\circ$=107Å). The first contours are at 2.5σ above the mean background level, while subsequent contours are at levels of 1.5nσ. For all images presented, north is at the top and east is to the left, and the centroid of continuum component A defines the origin.

Fig. 2.— A logarithmic grayscale representation of the line-emission (top panel) and continuum (bottom panel) images of 3C 34. The 20 cm radio contour map of Neff et al. 1995, whose spatial resolution of $1''4$ FWHM beam is comparable to that of our images, is superimposed on the [O II] frame. The line-emission image consists of the sum of 18 Fabry-Perot frames obtained across the line profile. The continuum image has a rest-frame wavelength of $\lambda_\circ$=4033Å ($\Delta\lambda_\circ$=107Å).

Fig. 3.— Intensity cross-sections of 3C 34. The top three panels show the [O II] line-emission for the three major regions of this source; the eastern emission-line region (components b and c), the central section (components A and B), and the western region (component a). The bottom panel shows the continuum profiles of component A and a nearby star (dotted line). The three cross-section cuts, east, center, and west, are shown in the inset line-emission contour plot. All positions are given as straight-line distances from the central continuum peak. It should be noted that the x-axis distance scale of each plot, with the exception of the central continuum and line-emission plots, are different from one another. Also, the smoothness of these curves is partly due to the rebinning of the data, such that only every second data point is independent.

Fig. 4.— [O II] line profiles at the positions of the major components labelled in figure 1, and at the diffuse emission between components b and c (b-c). Each profile is an average over 4×4 pixels in units of counts per pixel above the continuum.

Fig. 5.— A colour representation of the radial velocities (top panel) and the deconvolved velocity widths (bottom panel) of the [O II]λ3727 line-emission in 3C 34. The axes are labelled in arc seconds from the origin defined by the optical continuum emission peak A (shown with a cross). At the bottom of each panel a gradient scale is given matching the diagram's colours to velocities in $\mathrm{km\,s}^{-1}$. On the velocity map we also show the axes used for the cross-sections given in figure 6. The lengths of the cuts are given in figure 3.

Fig. 6.— The velocity profiles (top panels) and the deconvolved velocity widths (bottom panels) along three major axis cuts of 3C 34. The three panels for each of velocity and FWHM are divided into the eastern, central, and western regions defined in figure 3. The position and velocity origin has been taken to be at the radio galaxy center (component A).

Fig. 7.— Our proposed photoionization cone superimposed on the grayscale [O II] image of 3C 34. The dashed line indicates the radio source axis, as measured from the outermost hotspots of the 20 cm map shown in figure 2. The apex of the cone is located at the position of the central continuum source A; the location of the hidden AGN. An opening angle of $60°$ is the minimum required to photoionize the observed line-emission.

Fig. 8.— A schematic view perpendicular to the line-of-sight to 3C 34, looking *into* the eastern radio lobe of this source. In our model, the gas of the eastern line-emission region has been swept up by the southern end of the expanding radio lobe. The greater column depth along our line-of-sight to the bottom of the line-emission region results in a higher [O II] surface brightness on the outer side of this feature.

Fig. 9.— An **artificial** continuum image of 3C 34 as it would appear if each of the line-emission components were the result of an underlying starburst. Each starburst has been marked with the label corresponding to its associated line-emission component. With the exception of components a and b, in which continuum emission exists in the original image, components B and c are prominent and located in regions previously devoid of comparable continuum emission. Each starburst was given the same PSF as its associated line-emission component. This contour map should be compared with the observed continuum image shown in figure 1b.

Table 1: Properties of 3C 34 Continuum and [O II]λ3727 Components

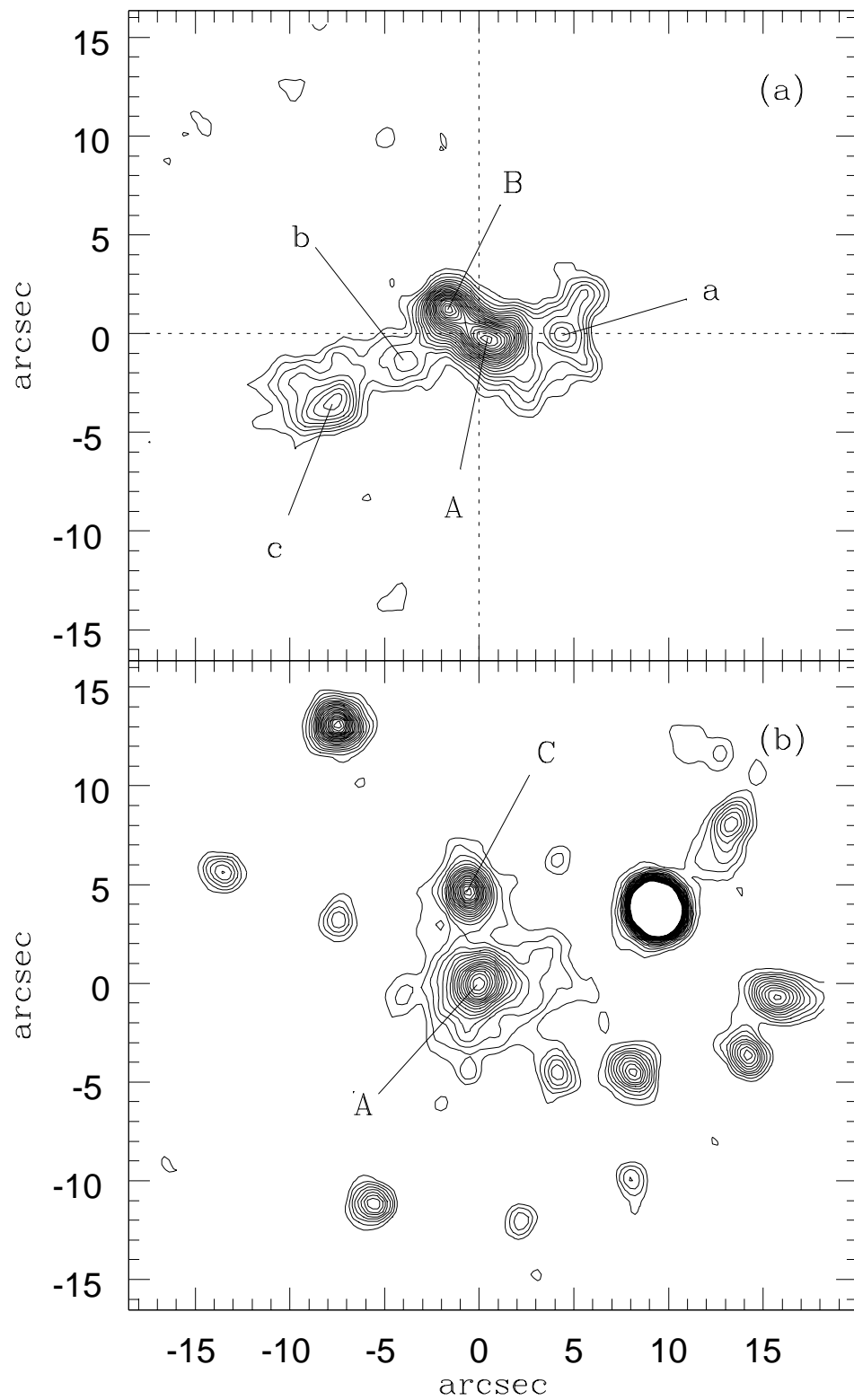| comp.	rel. pos. $\Delta\alpha$	$\Delta\delta$	r^a kpc	redshift	m_{4033}	M_{4033}	f([O II]λ3727)^b ($R_{aperture}$)	FWHM^c Å
All	—	—	—	0.689	—	—	223 (9.6)	38.7
A	0$''$0	0$''$0	0.0	0.6900±0.0007	20.68	-22.7	62.3 (1.8)	17.6
B	1$''$4	1$''$3	15.3	0.6899±0.0007	—	—	45.3 (1.6)	18.7
C	0$''$5	4$''$3	34.5	—	21.67	-21.7	—	—
a	-4$''$3	0$''$1	34.1	0.693±0.001	—	—	18.6 (1.4)	19.5
b	3$''$6	-1$''$1	30.1	0.687±0.001	—	—	12.3 (1.4)	14.4
c	7$''$1	-3$''$1	61.4	0.6881±0.0008	—	—	29.4 (1.9)	12.6

^{a} H$_\circ$=50 km s^{-1} Mpc^{-1} q$_\circ$=0.5
^{b} flux in units of 10^{-16} erg s^{-1}cm^{-2}(radius of aperture in arcsec)
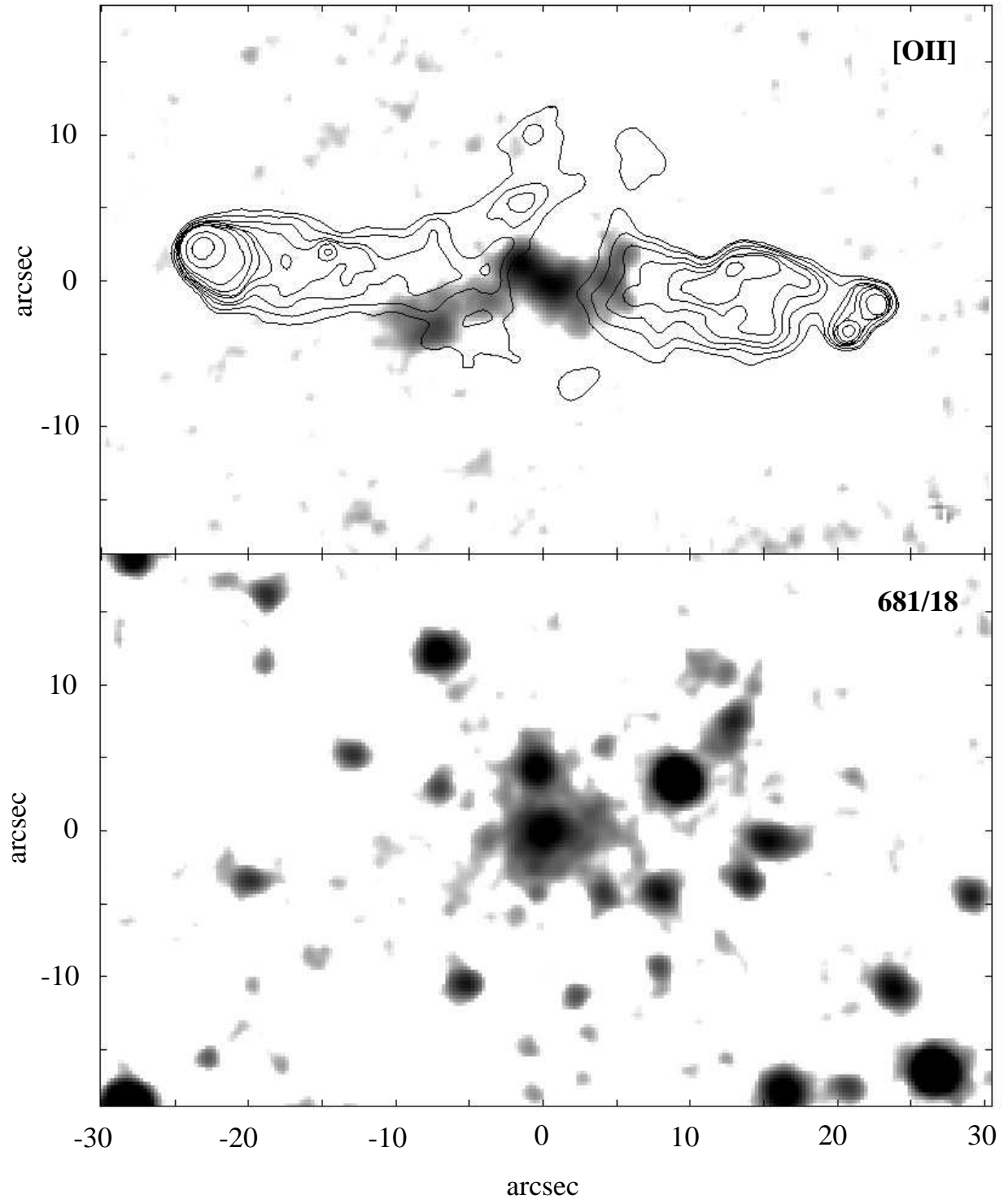^{c} observed FWHM corrected for instrumental broadening

Table 2: Results of Photoionization Calculations for 3C 34

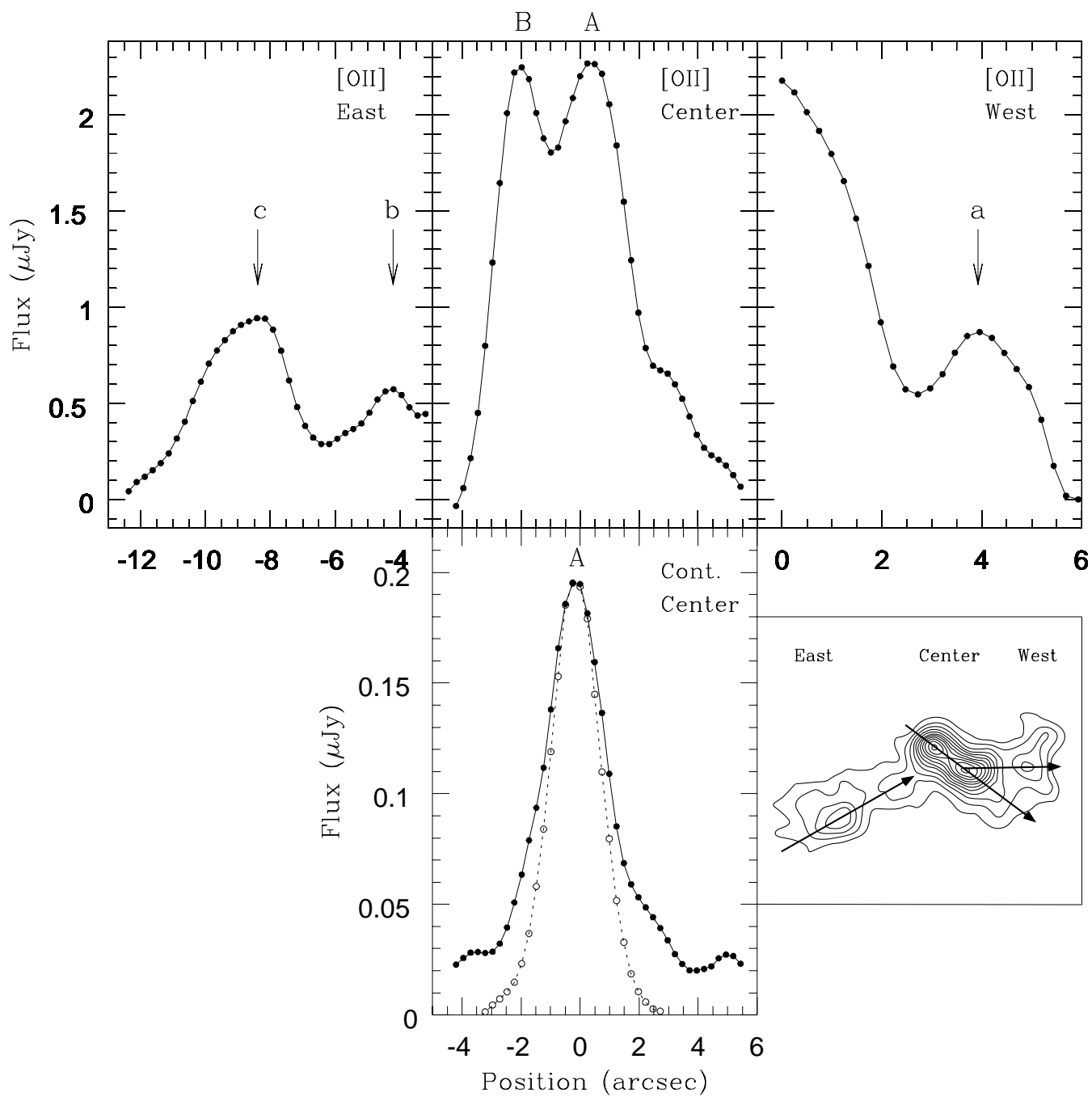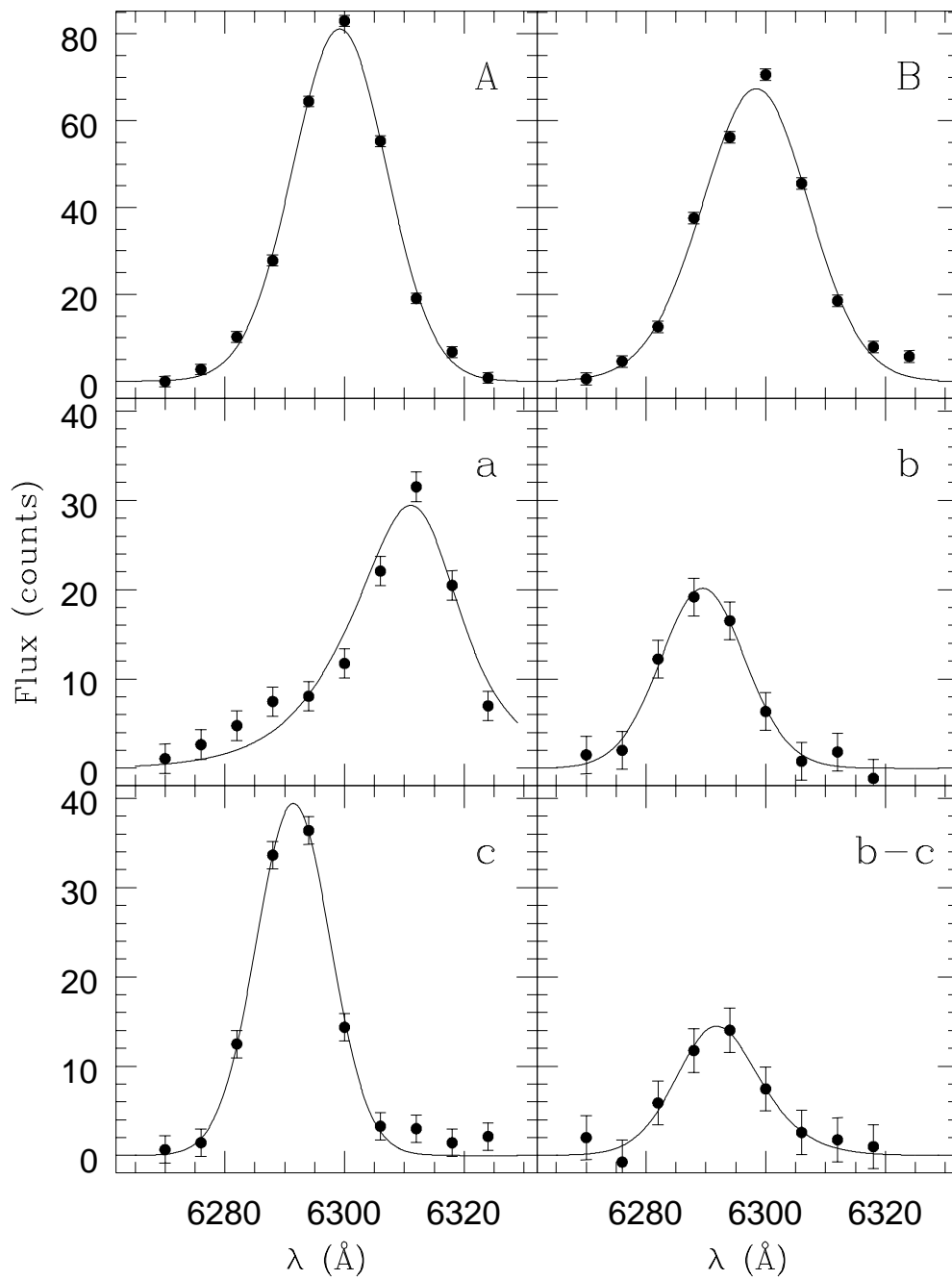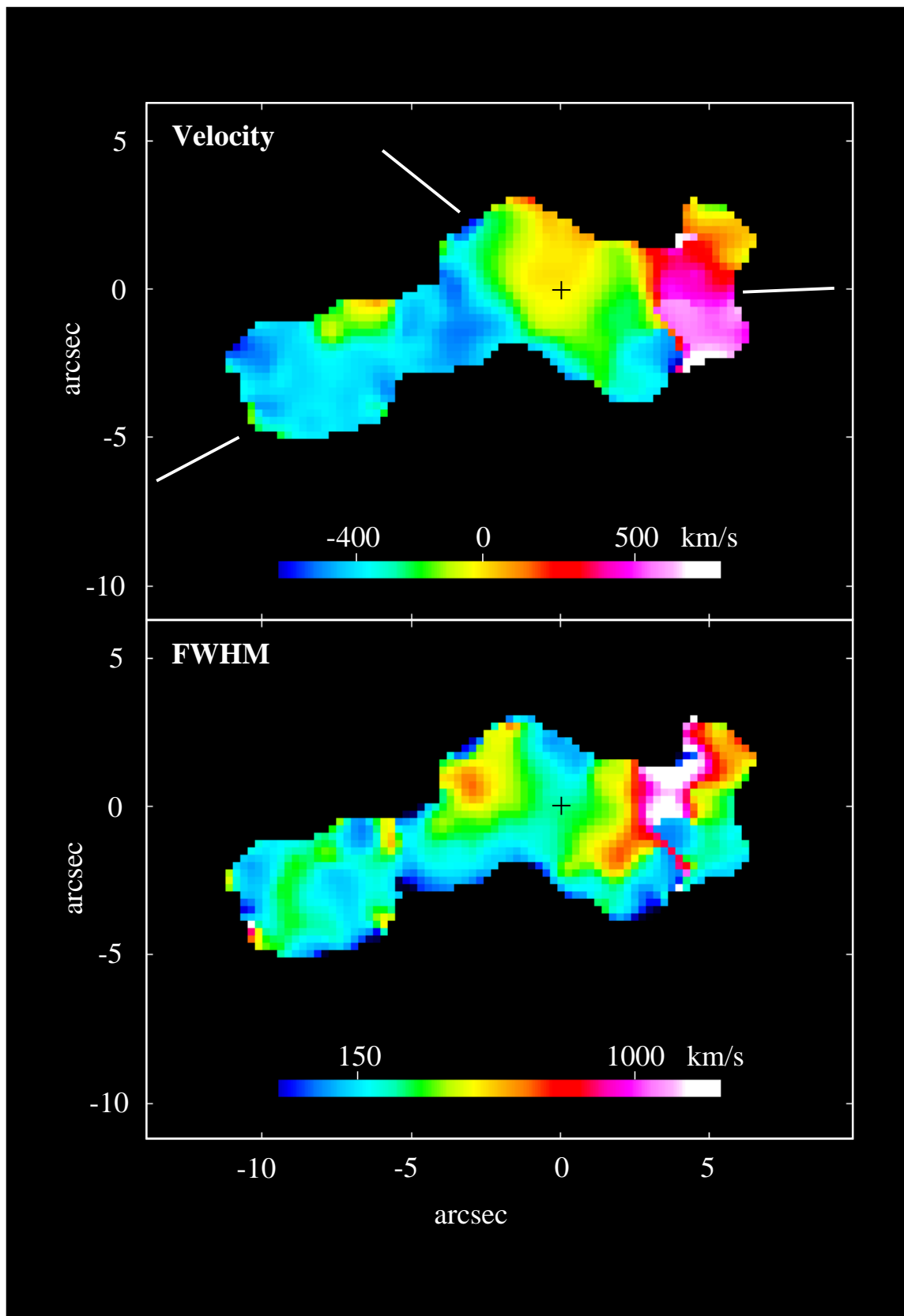| Source	Dist from AGN (")	Cone Opening Angle	Cloud Radius (")	L$_B$ AGN (erg s^{-1})	m$_v$ AGN
B	1.9	60°	1.02	1.4×10^{44}	19.5
			1.60	9.3×10^{43}	20.0
		88°	1.02	2.8×10^{44}	18.8
			1.60	1.8×10^{44}	19.3
c	8.2	60°	1.20	1.1×10^{45}	17.3
			1.90	8.0×10^{44}	17.6
		88°	1.20	2.2×10^{45}	16.5
			1.90	1.5×10^{45}	16.9

Figure 1: Neeser et al.
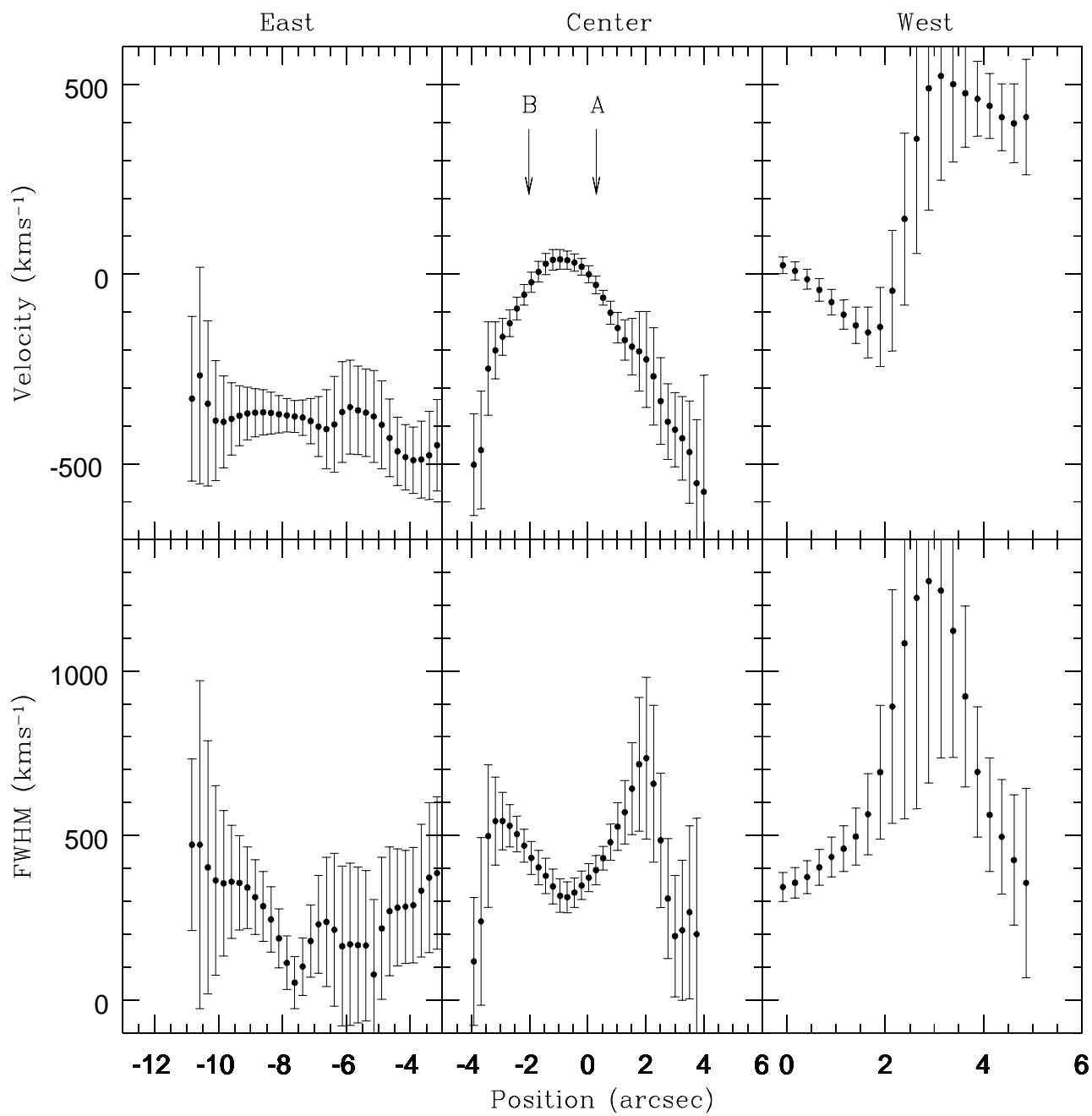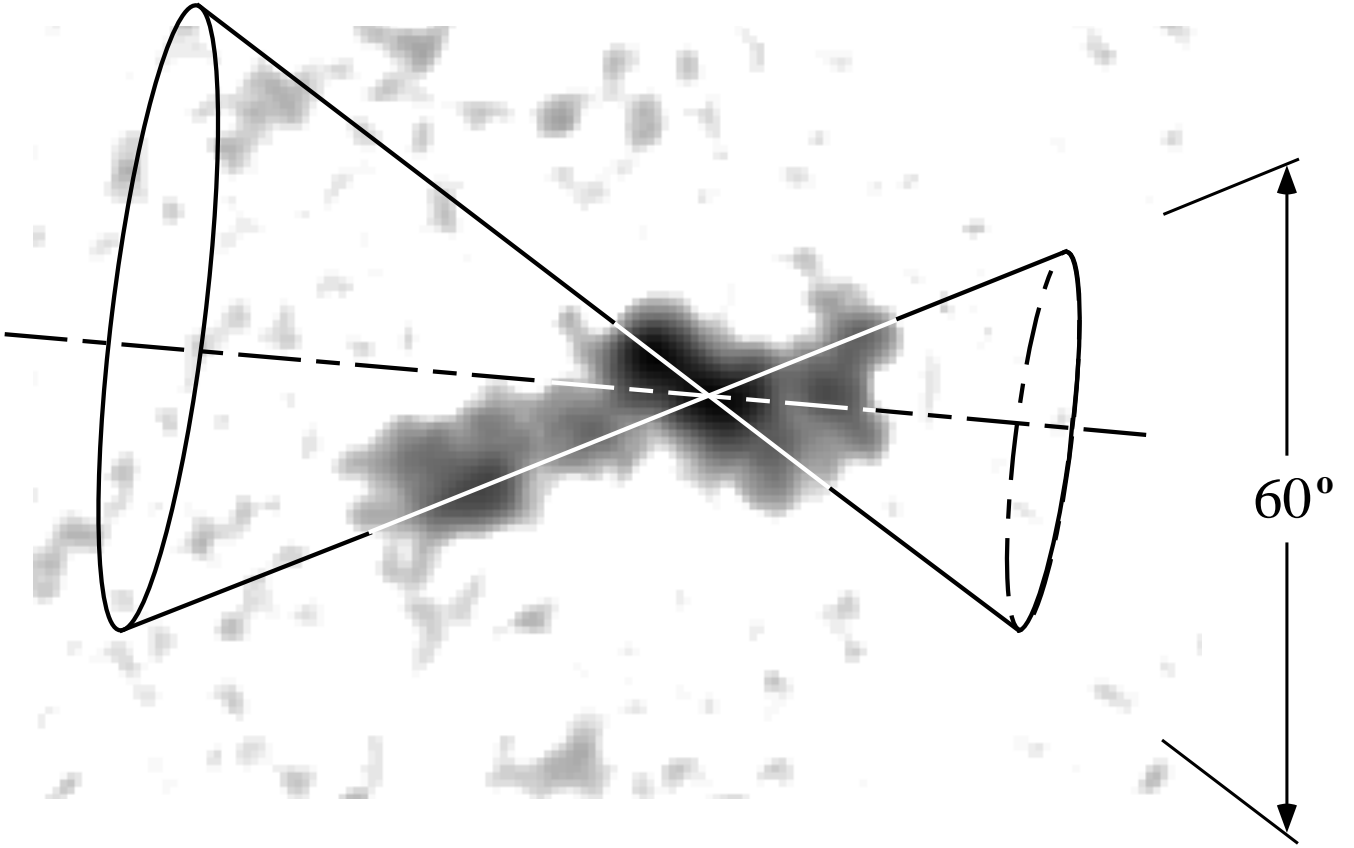
Figure 2: Neeser et al.

Figure 3: Neeser et al.
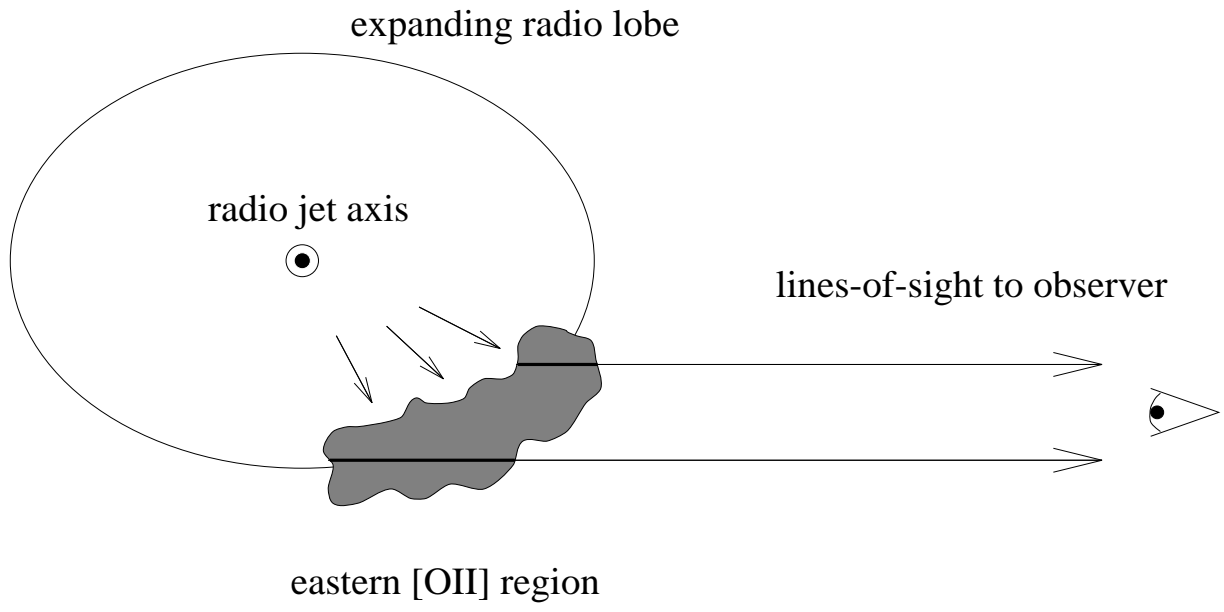
Figure 4: Neeser et al.

Figure 5: Neeser et al.

Figure 6: Neeser et al.

60°

Figure 7: Neeser et al.
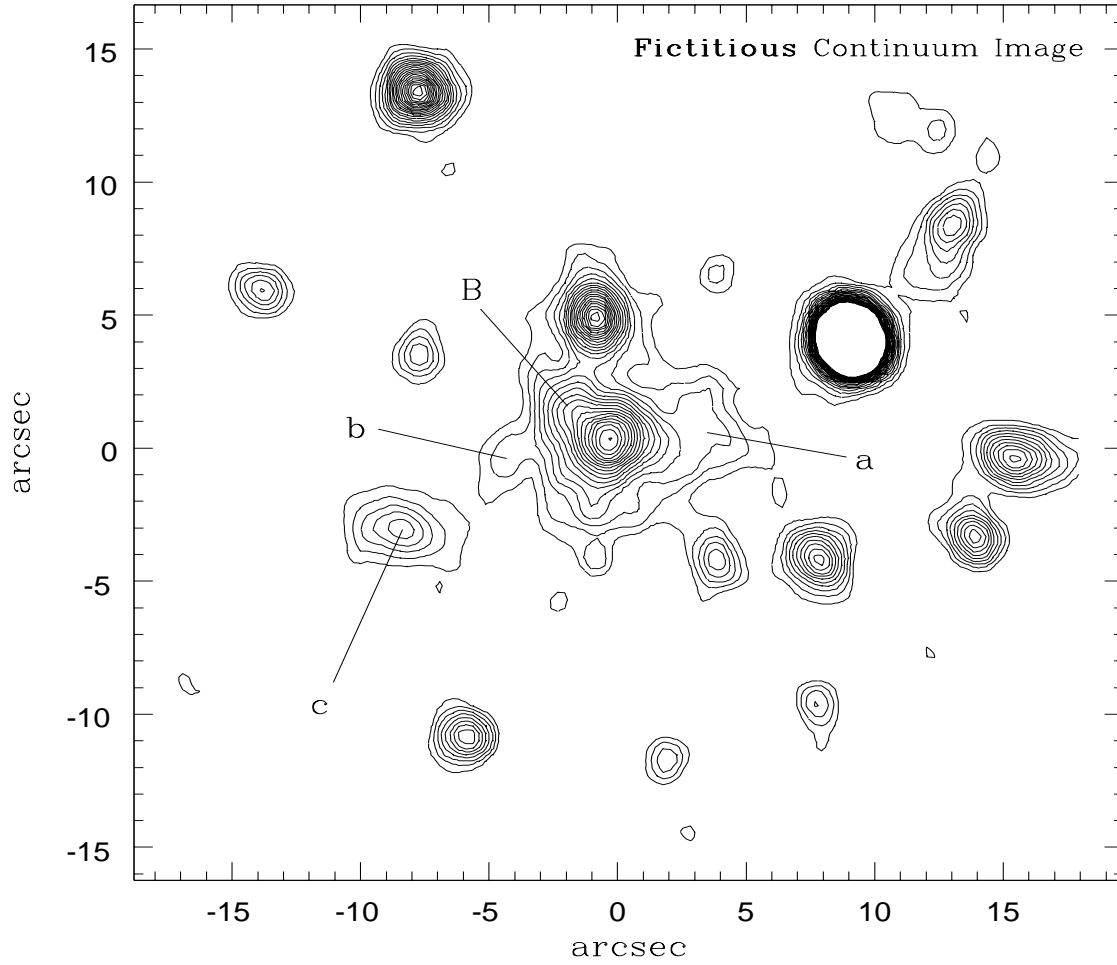
expanding radio lobe

radio jet axis

lines-of-sight to observer

eastern [OII] region

Figure 9: Neeser et al.

A Detailed Study of the Complex
Line-Emission Regions in the Radio Galaxy 3C 34

Mark J. Neeser[1], Klaus Meisenheimer, and Hans Hippelein

Max-Planck-Institut für Astronomie, Königstuhl 17, 69117 Heidelberg, Germany

ABSTRACT

We present the results of an extensive Fabry-Perot investigation of the extended line-emission gas surrounding powerful radio galaxies. High spatial ($\lesssim 1''4$) and kinematical ($400\,\mathrm{km\,s^{-1}}$) resolution observations of the [O II]$\lambda 3727$ emission-line of the powerful, double radio source 3C 34 (z=0.689) are given. We present evidence that anisotropic radiation emanating from a hidden AGN is responsible for photoionizing a line-emission region extending more than $120\,\mathrm{kpc}$. This is indicated by the distinctively bi-conical morphology of 3C 34's [O II] gas. A number of line-emission components may also show various degrees of 'shadowing' outward from the central ionizing source. A simple photoionization model is used to show that this interpretation is energetically viable on these length scales. The luminosity of the hidden central AGN, necessary to account for the observed [O II] luminosity, is compatible with that of a typical 3CR quasar at a similar redshift. Although this interpretation can account for the excitation and most of the unique shape of the warm gas, it is insufficient to explain the velocity and line-width structures observed with our Fabry-Perot. Therefore, we also propose that the illuminated medium surrounding 3C 34 is the result of gas swept up by the lateral expansion and backflow of the radio source lobes.

Subject headings: galaxies: active — galaxies: individual (3C 34) — galaxies: ISM — galaxies: emission-lines

---

[1]e-mail: neeser@mpia-hd.mpg.de

1. Introduction

The distant radio galaxy 3C 34 (z=0.6897) has a remarkable extended emission-line region, whose size (140 kpc) and brightness make it ideally suited to an in depth morphological and kinematical investigation. A number of high quality radio maps of 3C 34, primarily at 6 cm and 20 cm, can be found in the literature (*e.g.* Jenkins et al. 1977; Garrington et al. 1991; Neff et al. 1995; Johnson et al. 1995). These maps show this powerful radio galaxy to be a relatively symmetric, edge-brightened, $45''$ classical double. The first definitive optical identification of 3C 34 was made by Riley et al. 1980, who detected a faint, diffuse object located between the two brightest radio features. Although the detection of a strong [O II]λ3727 emission-line was sufficient to determine the redshift of this galaxy, the only other feature evident on the spectra of Spinrad 1982 is a very weak [Ne III]λ3869 line. The r_s-filter and intermediate-band imaging of McCarthy et al. 1995 reveal a galaxy in a rich compact cluster environment, and an extended region of high surface brightness [O II]λ3727 that is aligned with the radio source. This is also evident in the higher spatial resolution narrow-band [O II] and I-band continuum images presented by Johnson et al. 1995. Follow-up long-slit spectroscopy (McCarthy et al. 1996) of moderate quality detected both [O II]λ3727 and [O III]λ5007 emission, and allowed a rough velocity profile to be fit to the central region of 3C 34.

3C 34 is a spectacular example of the positional coincidence between the optical line-emission and the radio source axis, discovered to be a common phenomena in powerful, high redshift radio galaxies (McCarthy et al. 1987; Chambers et al. 1987). The combination of the novelty of this 'alignment effect', with the often spectacular morphologies of extended emission-line regions, and their potential effects on the evolution and formation of radio galaxies, attracted lively debate, little consensus, and a large number of possible explanations for this phenomenon. However, since the line-emission regions in high redshift radio galaxies, by virtue of their large intrinsic luminosities and large spatial extents, provide one of the best methods for probing the warm gas at early epochs and across a broad range of redshifts, the importance of understanding the alignment effect cannot be understated. Since this phenomena arises in extended, highly dynamic gas, an investigation that combines well-resolved morphologies with kinematics would go far in shedding new light on the question of the origin of the line-emission gas, its excitation, and the cause of the alignment effect. We therefore began an in depth survey of the [O II]λ3727 line-emission in 11 radio galaxies ($0.45 \lesssim z \lesssim 1.1$) using a Fabry-Perot etalon. This instrument produces seeing-limited maps of both the morphological and kinematical structure of these line-emission regions. We continue with the presentation of this data by describing our results for the powerful, high redshift radio galaxy 3C 34.

This paper has been organized as follows. In the first section we present the observations and the data reduction. In section 3 we give a qualitative description of the emission-line and continuum morphologies, and the kinematics of the [O II] gas. Our interpretation of this data, in terms of a model to account for the ionization, origin, and kinematics of the warm gas in 3C 34, is discussed in section 4. This section concludes with an account of alternative

models. In order to compute physical sizes, 'proper' distances, and luminosities, a standard Friedmann-Robertson-Walker cosmology with a zero cosmological constant, $H_o = 50\,\mathrm{km\,s^{-1}\,Mpc^{-1}}$, and $q_o = 0.5$, have been assumed throughout this paper. At the redshift of 3C 34 this results in a luminosity distance of $1.44 \times 10^{28}\,\mathrm{cm}$ and an angular scale of $7.94\,\mathrm{kpc\,arcsec^{-1}}$.

2. Observations

2.1. Observations of 3C 34

The Fabry-Perot and continuum images of 3C 34 were obtained on Sept. 1991 and Sept. 1992, respectively, at the prime focus focal reducer of the 3.5 m telescope on Calar Alto, Spain. The [O II]λ3727 imaging spectroscopy was done with a GEC chip having 22.5μm pixels, giving a 'plate' scale of $0\rlap{.}''49$/pixel. We observed 3C 34 at 10 different wavelength settings between 6270Å and 6324Å, separated by 6Å steps. Multiple exposures of 1200 seconds each were made at every wavelength step, and resulted in 22 individual Fabry-Perot images. This allowed complete coverage of the redshifted [O II]λ3727 line. An interference order 30, corresponding to an instrumental profile width FWHM of $\Delta\lambda=8.3$Å, was chosen to give a spectral resolution of $395\,\mathrm{km\,s^{-1}}$. The resulting [O II] images of 3C 34 ranged in seeing from $1\rlap{.}''1$ to $1\rlap{.}''7$ FWHM, with a median value of $1\rlap{.}''3$. To investigate the continuum morphology, as well as subtract its contribution to the [O II] images, line-free continuum exposures were obtained immediately redward of our [O II]λ3727 observations. These were taken at $\lambda=6811$Å ($\Delta\lambda=180$Å), and correspond to $\lambda_o=4033$Å ($\Delta\lambda_o=107$Å) in the rest frame of the radio galaxy. A total of five exposures of 500 seconds each were obtained in this continuum filter using a TEK chip with 24μm pixels and a resulting image scale of $0\rlap{.}''53$/pixel.

2.2. Data Reduction

Since the reduction procedures unique to Fabry-Perot (FP) images are described in detail in Meisenheimer & Hippelein 1992, we will give only a brief summary of the processing steps applied to the data obtained for 3C 34. The initial reduction followed that of standard CCD data processing: bias subtraction, dark current correction, flat fielding done using dome flat exposures obtained at the wavelength of each Fabry-Perot science image, and the removal of cosmic ray events. Further reduction steps, peculiar to FP imaging and necessary to extract the kinematical information, are briefly summarized.

(i) Night sky emission-lines (in particular, OI at $\lambda\simeq6300$Å) cause a 'ring' of enhanced background on each Fabry-Perot image at wavelengths shortward of the observed wavelength. An interpolation of the background pixels (defined from the local background level of each frame and a user-given σ–clipping) resulted in a fit of the radial profile of this emission. This background fit was smoothed in its radial and azimuthal directions and subtracted from each Fabry-Perot frame.

(ii) The alignment and relative scaling of all frames was based on a comparison of positions, profiles and intensities of 10 field stars of intermediate brightness. Since our subsequent spectral analysis of the [O II] line was done over the entire range of sampled wavelengths and included 22 individual frames, the degree of alignment between individual images needed to be better than $\sim 0\rlap{.}''05$ to prevent a cumulative positional error from becoming unacceptably large. This level of alignment was ensured by computing frame differences, examining the residual star images, and interactively adjusting the frame shift, rotation, and scale, until the desired overlap accuracy was achieved. The relative intensity scaling of each Fabry-Perot frame, with respect to the reference image, followed by requiring that the average continuum source in the field (*i.e.* the 10 reference field stars) showed a flat spectrum across the wavelength range covered by the Fabry-Perot images. This allowed us to adequately reduce the influence of possible intensity gradients, characteristic of some late-type stellar spectra, in our determination of the normalization constant.

(iii) In order to transform all of the Fabry-Perot and continuum images to a common positional reference frame and a common effective point spread function (PSF), a two-by-two pixel rebinning was done for all exposures. The FWHM chosen for the PSF convolution ($1\rlap{.}''65$) was somewhat broader than the FWHM of the Fabry-Perot image having the worst seeing. The result of this rebinning was a set of images with zero positional offsets, identical intensity normalizations, identical circular PSFs, and a pixel scale of $0\rlap{.}''247$ pixel^{-1}. To obtain pure line-emission images the scaled and rebinned continuum frame was subtracted from each Fabry-Perot image.

(iv) These line-emission images were then stacked into a cube with wavelength as the third dimension. A fit of a single Gaussian profile was made through this cube at each pixel of the source, when the total line flux in each pixel exceeded a given threshold. The output of this spectral fitting analysis consisted of six 2-dimensional frames containing the peak amplitude of the line-emission, the wavelength value of this maximum, its e-folding width, and the rms errors associated with each of these parameters. From these fit parameters we were then able to compute the the relative velocity and the FWHM of the [O II]λ3727 line-emission at each pixel.

(v) Standard aperture photometry techniques were used to determine the counts–to–flux conversions from the observed standard star, and used to photometrically calibrate the continuum and FP images. Observations of the calibration standard were only made at the central FP wavelength (λ=6294Å) setting. However, since the remaining Fabry-Perot images were scaled to this wavelength (step (ii)), a calibration of the entire [O II]λ3727 line could be made. Using a generalized non-linear least-squares curve these flux points were fit to a Gaussian profile by varying the amplitude, central wavelength, and standard deviation of the Gaussian profile until an optimum fit, indicated by a minimized χ^2, was achieved. The outermost wavelength points were assumed to sample only the continuum emission from the source, and hence the fit was forced to be flat at this level. The total line-emission

flux was then calculated by assigning the absolute value of the flux density obtained for the central wavelength frame to the amplitude of the fit, and integrating the profile across the line. The statistical uncertainty assigned to the flux density and the profile width were found by separately varying the amplitude and the standard deviation of the Gaussian fit, respectively, until χ^2 was increased by one for each parameter. We estimate a typical formal uncertainty in our determination of the total [O II] line flux to be better than 20%. Due to the Galactic latitude of 3C 34 ($b \simeq -31°$), no extinction correction for Galactic reddening was necessary (E(B–V) < 0.03, Burstein & Heiles 1982).

3.   Results

3.1.   Morphology

The continuum and line-emission images of 3C 34 are shown as contour maps in figure 1 with the components discussed in the text labelled.

3.1.1.   Emission–Line Morphology

The [O II] line-emission morphology of 3C 34 is spectacular in both its extent and complexity. The continuum-subtracted [O II]λ3727 grayscale image of 3C 34 is shown in the top panel of figure 2. The central region is dominated by a double-lobed, high surface brightness feature characterized by the two emission peaks, A and B. We identify the brightest line-emission source (component A) with the radio galaxy, as it is displaced by only $\simeq 0''\!.3$ to the southwest of the central continuum source (see figures 1 and 3). In contrast, the line-emission peak at B is not associated with an underlying continuum source, and has an intensity cross-section that is indistinguishable from a stellar profile. A further difference between these two components is that the line-emission falls off steeply and ends abruptly to background flux levels toward the northeast of source B. The outer end of component A levels off and merges with a faint finger line-emission extending a further $2''\!.5$ beyond the southwestern end of this central [O II] component (see figure 3).

Almost directly to the west of component A lies another [O II] knot, component a. This source is at the apex of a unique V-shaped structure that opens toward the west, away from the radio galaxy center. It is particularly interesting that these two fingers of emission extend symmetrically from either side of the line connecting component a with the central radio galaxy, and also lie on either side of the central axis of the western radio lobe.

The eastern side of 3C 34 is the most extended and contains two further knots of line-emission, components b and c. Component b sits close to the double-lobed central feature, but marks a sudden change in direction by being almost perpendicular to the major axis defined by components A and B. Further westward from component b is the strongly asymmetrical knot c, whose contours

are noticeably compressed in the direction toward the radio galaxy center, and stretched in the opposing direction. This is particularly evident in the intensity cross-section of the eastern region shown in figure 3. These steep contours also continue around to the south of component c, but strongly fan out toward the west and north of this source. On this side the surface brightness of component c gradually diminishes to the fainter flux levels of the eastern line-emission region.

The projected [O II] line-emission region of 3C 34 extends for an uninterrupted $18''$ or 144 kpc, placing it among the largest extended emission-line regions known. Despite this large overall size, the lateral extent of the line-emission is quite narrow and never exceeds roughly $5''$(41 kpc), giving 3C 34 an axial ratio of almost 1:4. It is interesting to note the overall twisted morphology of the emission-line region. Beyond the rather well-defined position angle of the central sources (components A and B), the fainter more extended line-emission to the east and west undergo radical changes in direction. Considering both the differences in surface brightness and orientation, the overall line-emission in 3C 34 can be divided into three distinct regions; the *central* component dominated by sources A and B, and the two outer *eastern* and *western* regions distinguished by knots b and c, and knot a, respectively.

To improve the objectivity in determining the position angle of our line-emission data we included only those pixels above a flux threshold of $3\sigma_{\rm sky\,rms}$, and computed the flux-weighted first and second moments of the [O II] image. This gave a position angle of $103° \pm 1°$for the extended emission-line region of 3C 34. Comparing this to the orientation of the radio emission, as measured along the line connecting the outermost hotspots, 3C 34 is moderately well-aligned with ΔPA $= 18°$.

The pure [O II]$\lambda3727$ line-emission from 3C 34, within a circular aperture of $9\!''\!.6$ radius, is 2.23 $\times 10^{-14}\,{\rm erg\,s^{-1}cm^{-2}}$. For the cosmological parameters defined in the introduction this translates to a total [O II]$\lambda3727$ luminosity of

$$L_{[OII]} = 5.8 \times 10^{43} \ \ {\rm erg\,s^{-1}}.$$

If we assume that the observed [O II] emission originates in a plasma with temperatures of about 10^4 K, in which the most abundant oxygen ion is O$^+$, then the gas density can be related to the [O II]$\lambda3727$ line luminosity by

$$L_{[\rm OII]} = 2.3 \times 10^{41} \ n_e^2 \ \zeta \ f_v \ V_{\rm kpc} \ \ {\rm erg\,s^{-1}} \tag{1}$$

(Osterbrock 1989). Here n$_e$ is the electron density in cm^{-3}, ζ is the oxygen abundance relative to the solar value, f$_v$ is the volume filling factor of the line emitting gas, and V$_{\rm kpc}$ is its volume in kpc^3. Assigning a value to the degree of 'clumpiness' of the gas is the greatest uncertainty in determining the overall density, with filling factors ranging from 3×10^{-4}, as measured from [SII] line ratios in low redshift radio galaxies (Heckman et al. 1984), to 2×10^{-6} for line-emitting gas associated with cooling flows (Heckman et al. 1989). Taking a volume of 5.1×10^4 kpc^3, a filling factor midway between the observed extremes (10^{-5}), and a relative oxygen abundance of 0.03, gives an average density of the [O II]$\lambda3727$ gas of n$_e \sim 130$ cm^{-3}. If we assume that the gas in

3C 34 is completely ionized, the average density and volume computed above give a total mass of warm gas in 3C 34 of $M_{gas} \sim 2 \times 10^9$ $M_\odot$.

3.1.2. Optical Continuum Morphology

3C 34 is equally spectacular in the light of our deep line-free continuum image. This galaxy appears to lie in a rich, compact cluster, with 18 possible companion galaxies within a radius of 200 kpc of the central source (see figures 1 and 2). With the exception of component A, however, we do not detect [O II]λ3727 line-emission from any other continuum source in the field despite a Fabry-Perot velocity coverage of $-1600 \, \mathrm{km \, s^{-1}} \leq \Delta v_\circ \leq +1300 \, \mathrm{km \, s^{-1}}$, in the rest frame of the central galaxy. In fact, the many continuum sources surrounding the central radio galaxy appear to avoid the contours associated with the line-emission image.

Near to the center of the cluster lies the brightest source, component A. This galaxy is positioned almost exactly at the center of the radio emission and is identified as the optical counterpart to the radio source (Riley et al. 1980). From the line-emission associated with component A we compute a redshift for this central source of z=0.6900 $\pm$ 0.0007. As is evident from figure 3, the core of component A is only marginally different from a stellar profile. However, beyond a radius of about $2''$ A appears to be embedded in a broad continuum halo, within which a number of faint knots of emission can be seen. The central continuum component A, as derived from our continuum frame and 17 reference stars from the PPM catalogue (Röser & Bastian 1991), has an absolute position of

$$\alpha = 01^{\mathrm{h}} \, 07^{\mathrm{m}} \, 32\overset{\mathrm{s}}{.}55 \qquad \delta = +31° \, 31' \, 22\overset{''}{.}8 \qquad (1950.0),$$

with an uncertainty of $\pm 0''5$ in both coordinates. This position was used to place the radio contours in figure 2 and agrees to within $0''6$ of the radio nucleus detected in the $\lambda 6$ cm and $\lambda 20$ cm observations of Johnson et al. 1995.

To the north of the radio galaxy lies a close (at least in projection) companion galaxy, component C. Although this companion is close enough to component A to share its outer halo emission at the lower flux levels, it is undoubtably a distinct source. Inspection of the line-emission images at the faintest flux levels and at all wavelengths, revealed no [O II]λ3727 counterpart to this continuum source. Therefore, we cannot assign a redshift to this component.

In contrast to the line-emission image, the crowded continuum environment of 3C 34 makes an unequivocal determination of the position angle of the host galaxy difficult. Beyond a radius of $\sim 3''$ from the central radio galaxy the position angle changes sharply, as a number of companion sources, in particular component C, enters the aperture. However, since the companion source C is distinct from the radio galaxy at the brighter flux levels with no associated [O II]λ3727 detection, we determined a position angle that is confined to the direct environment of component A. Within an aperture of $3''0$ radius centered on this source, with component C subtracted from the image,

the continuum position angle was found to be $106° \pm 5°$. Thus the continuum emission is well aligned with the line-emission (ΔPA(|line–continuum|)=3°) and only moderately aligned with the radio source (ΔPA(|radio–continuum|)=21°).

In table 1 we present a synopsis of the relative positions, physical separations, continuum magnitudes, [O II]λ3727 flux levels, and FWHM of the continuum and line-emission components observed in 3C 34.

3.2. Kinematics: Radial Velocities and Deconvolved Line Widths

Figure 4 illustrates line profiles at specific positions in the line-emission region of 3C 34. The velocity map obtained from the fit to the Fabry-Perot data cube is shown in figure 5, with the velocity and FWHM profiles along the three major regions of 3C 34 shown in figure 6. The kinematical and positional origins of figures 5 and 6 are defined by the radio galaxy center. Compared to the other sources in our overall sample the range of velocity spanned by 3C 34, in particular considering the extreme size of its emission-line region, is quite moderate. The dynamical structures visible in this source, based on their shape and absolute velocity, can be divided into the same three distinct regions that were used in describing the line-emission morphology. The velocity of the [O II] gas in the central region of 3C 34 (figure 6 central panel) is distinguished by a relatively smooth velocity bump spanning $0 \, \mathrm{km \, s^{-1}}$ near the center of this region, to -500 $\mathrm{km \, s^{-1}}$ at its northeast and southwestern ends. The line-emission sources A and B are positioned on either side of this feature. The corresponding line widths show an obvious minimum at the position of this velocity peak, which is $\sim 1''$ to the northeast of component A. This local FWHM minimum is at $300 \, \mathrm{km \, s^{-1}}$ and rises steadily away from both A and B to $\sim 750 \, \mathrm{km \, s^{-1}}$ and $550 \, \mathrm{km \, s^{-1}}$ respectively. The subsequent decline in the FWHM observed in figure 6, beyond about -3$''$ and +2$''$, may be due to low flux levels resulting in poor fits to the data cube, or to a slight over-subtraction of the continuum.

The eastern region of 3C 34 is surprisingly flat at velocity values near $-400 \, \mathrm{km \, s^{-1}}$. The fact that the deviations from this velocity value are always less than about $150 \, \mathrm{km \, s^{-1}}$ is remarkable considering that this side of the source spans more than 70 kpc of projected line-emission. The associated velocity widths of this region reveal a number of low significance undulations. The FWHM on this side of the 3C 34 are the lowest for the entire source and, in an absolute sense, the average FWHM ($\lesssim 250 \, \mathrm{km \, s^{-1}}$) of this region is remarkably quiescent.

To the west of 3C 34 we observe a very sudden velocity change in going from the gradual decline still visible from the central region, out to component a. This velocity discontinuity spans about $690 \, \mathrm{km \, s^{-1}}$ from the western end of the central region to the beginning of source a. This is most evident in our two-dimensional velocity images (figure 5) and points to the fact that we are seeing an overlap of two distinct sources (*i.e.* component A and component a). This superposition of sources results in the large FWHM seen at this position. At the location of component a, we

see the maximum overall velocity for 3C 34 (v=500 km s^{-1}). Across the remainder of the western region the velocity remains relatively flat.

4. Discussion

4.1. Photoionization by a Hidden AGN

Most noteworthy about the morphology of 3C 34 is that the line-emission exhibits a bi-conical shape with the nucleus of this radio galaxy at the apex of the cones. We will argue that this unique shape is the result of an ambient medium swept aside by the radio source, and subsequently illuminated by a collimated source of ionizing radiation.

Since the likeliest location of the active nucleus lies at the centroid of continuum component A, we will designate this as the origin of the cone. We will also assume the photoionization cone to be close to the plane of the sky; an assumption consistent with the narrow gap between the radio lobes and the evidence for jets on both sides of the source (Johnson et al. 1995). As is shown in figure 7, it then immediately follows that a straight line can be drawn from the peak of component c, through the origin, to the peak of the finger of emission northwest of component a. Similarly, a straight line can be drawn through component B, the origin, the line-emission component A, and the center of the faint extension of line-emission at the southwestern end of component A. Thus, simply by placing the apex of a symmetrical bi-cone at the position of the central continuum source, we find that we can connect 6 distinct line-emission knots/extensions on both sides of 3C 34 and symmetrically straddle the radio source axis. Drawn in this way, the bi-cone has an opening angle of 60°. However, since it is defined by the positions of the peak intensities of the brightest emission-line components, the true opening angle necessary to photoionize all of the [O II] gas may be somewhat larger. A bi-cone drawn through the same center, but using the outer FWHM positions of components B and c, results in an opening angle of about 90°.

Such a conical structure in 3C 34, though unobserved in high redshift radio galaxies, has been observed in low redshift Seyfert galaxies and in 3C 227 (z=0.085) (Prieto et al. 1993). Currently 11 such Seyferts are known to possess an ionization cone or a bi-cone—8 of which also contain a linear radio structure (*i.e.* a double, triple, or jet-like radio source) (Wilson & Tsvetanov 1994). From these sources Wilson & Tsvetanov 1994 find that there is a tight alignment between the cone and radio axes, with a mean difference in position angle of only 6°, and that the degree of collimation is much better for the radio plasma than for the ionizing photons. This is exactly what is observed in 3C 34. As in the Seyferts, the bi-cone of 3C 34 is situated almost exactly along the axis defined by the radio emission, with ΔPA = 4°. The prominent cones in Seyferts and 3C 227, however, show emission across the entire lateral extent of their opening angles (see, for example, the [O III]λ5007 image of NGC 5252 in Tadhunter & Tsvetanov 1989). This is not true for 3C 34, where the line-emitting gas appears to be confined to the outer edges of the ionization cone and by no means fills it.

Aside from explaining the overall conical morphology of 3C 34, the photoionization model can be applied to a number of smaller-scale features seen in line-emission. The intensity profiles of components c and a on the eastern and western side of the bi-cone, respectively, are both markedly steepened on their sides facing the central source (see figure 3). This could be due to geometrical dilution or by absorption or scattering in intervening material closest to the central source. It is also possible that radiative bounding of the ionizing flux from the central galaxy can give rise to the morphology seen in source B, and in the western component. The steep fall-off in intensity and the lack of any line-emission outward from component B points toward this source being a very dense knot of gas capable of absorbing all of the incident ionizing radiation. It is also plausible that component a is 'shadowing' the ionizing emission from the AGN, and preventing this flux from reaching the gas to its immediate west. The small lateral extent of source a may allow the ionizing radiation to reach the gas surrounding it to the north and south, causing the two fingers of [O II] emission observed extending to either side of component a. The ionizing radiation reaching the gas on the western side of 3C 34 could be somewhat diluted due to strong absorption occurring in the central component A. This would, in turn, allow component a to effectively absorb the remaining radiation and at the same time remain relatively faint. An alternative explanation for the fall-off in [O II] emission outward from components B and a could, of course, be a simple paucity of gas beyond these sources.

A critical test of our photoionization model is whether or not the central, hidden AGN can provide enough ionizing photons to excite the [O II] emitting gas observed in 3C 34. The two best line-emission sources on which to test this are component c, because it is furthest from the central galaxy, and component B, because it is the brightest source beyond the central galaxy. The very sharp fall-off in [O II] brightness on the side of component B facing away from the central source, argues for a region that is radiation bounded. Furthermore, since the [O II] flux integrated across the eastern component out to source c is almost identical to that observed for source B, we will assume that c is also radiation bound. Thus, a covering factor of unity will be used for these two sources.

A description of the model that we have used to estimate the luminosity of the central source, necessary to photoionize the observed line-emission regions, is given in the appendix. This model assumes that the central ionizing source has a spectral index of 1.0 and that the ratio of ionizing photons to resulting [O II]$\lambda3727$ photons is 6:1. Then, using equation A6 we have computed the required luminosity of the central source necessary to produce the [O II]$\lambda3727$ flux observed in components B and c. The results of this computation are summarized in table 2 using source radii based on both the FWHM and the total lateral extent of components B and c, and two different ionization cone opening angles. Clearly, component c is the most critical source due to its distance from the central galaxy. Even with the worst case parameters of a large 88° opening angle and a small radius, we conclude that the required luminosity of the hidden, photoionizing AGN is reasonable, at roughly a factor of three lower than the B-band luminosity of the brightest 3C quasar. If viewed along a line-of-sight down the ionization cone the apparent V-band magnitude

(see column 6 of table 2), assuming zero extinction, would be comparable to a typical 3C quasar at the redshift of 3C 34 (Allington-Smith 1984).

Of course, the evidence for photoionization in 3C 34 could be improved using line ratio diagnostics. For such tests a number of low-to-high ionization lines would have to be detected in the faint, extended line-emission region (*e.g.* component *c*). The literature shows, however, that even the detection of a sufficient number of lines in the considerably brighter nucleus has been difficult; the high ionization lines [Ne III]λ3869 and [Ne IV]λ3426 were found to be very weak and undetectable, respectively, in the spectrum of Spinrad et al. 1985, and Rawlings et al. 1991 failed to detect the [S III]λ9532 line in their near-infrared spectrum.

4.2.   The [O II] Kinematics and Radio Source Expansion/Backflow

The final issue that must be addressed is how the velocities observed in the [O II] gas of 3C 34 fit into the photoionization framework. The simplest model would assume that the ionization cone is merely illuminating gas clumps, of random velocity, that exist in a typical cluster environment. The abrupt velocity discontinuities between the central source and the two line-emission regions to the east and west would tend to support such a picture. The overall velocity spanned by the entire line-emission region is also consistent with a rich cluster (*e.g.* Dressler & Gunn 1992). The difficulties with this interpretation, however, arise when one considers that the [O II] line-emission in 3C 34 is uninterrupted across more than 140 kpc—unusual considering that the warm gas in a cluster environment is usually considered to be in discrete clumps or filaments unconnected over such large regions. Even more fatal to the cluster interpretation is the fact that the eastern component shows a remarkably flat velocity structure across a length of more than 70 kpc. Such uniformity across such large distances is incompatible with the essentially random velocity dispersions associated with clusters. In fact, the constant velocity across the entire eastern line-emission region would seem to indicate that a *single* mechanism is required to act on a large fraction of gas simultaneously.

As is clear from figure 2 the eastern line-emission region is near the outer edge of the radio source, and also seems to conform well to the radio contours. We therefore propose that the radio source has, through the bulk motions of its lateral expansion, enmasse swept up the gas that existed in the environment of 3C 34. In this way the gas that makes up the eastern [O II] line-emission region is compressed, pushed to the outer edge of the radio, and given a bulk velocity that is constant across the entire region. The connection between the radio lobes and the line-emission gas is corroborated by the orientation of 3C 34, independently deduced from the radio observations and our optical data.

Radio polarization measurements of 3C 34 by Johnson et al. 1995, find a higher degree of depolarization in the eastern radio lobe, particularly prominent along the position of the line-emitting gas. The western side of 3C 34, on the other hand, shows no similar match between

the location of its line-emission gas and depolarization in the radio lobe. This supports our radio lobe expansion and backflow interpretation of the blue– and redshift observed in the eastern and western line-emission regions; namely, that the line-emission to the east of 3C 34 is oriented toward us, while the western region points into the plane of the sky.

Lateral expansion in the radio source lobes may also be playing a significant role in defining the velocity observed in the western line-emission region. In this case its redshifted velocity with respect to the central galaxy could be due to the far side of the radio lobe expanding away from us and sweeping the gas along with it. The fact that the western line-emission region is symmetrical with respect to the radio axis may be due to the gas spreading both north and south as the far side of the radio lobe sheath expands. Alternatively, the western line-emission region, as is indicated by the velocity and line width discontinuity between this region and the central source, may simply be a distinct gas cloud that is being illuminated by the ionization cone of 3C 34. We are currently unable to distinguish between these two interpretations.

More difficult to explain is the velocity structure observed in the central line-emission region. The smooth velocity bump may indicate some form of mass inflow or outflow, whose asymmetry may be intrinsic, or due to some form of extinction that inhibits our view of the far-side velocity surface. Alternatively, if we assume that the radio lobes lie behind both the northeast and southwest ends of this component, but do not extend all the way to the center of the source (as seems to be indicated in figure 2), backflow and/or cocoon expansion could selectively push these ends toward our line-of-sight and create the observed velocity bump. Radio source backflow is indicated by the prominent 'wings' of radio emission near to the central source, that extend perpendicular to the major axis (see figure 2). The close correspondence between the radio source and the NE end of component B, as well as the velocity width maxima observed at the ends of both central components (see figure 5), could be the result of such an interaction. It is interesting to note that the NE line width maximum is not symmetric with respect to the major axis of the central component $(A + B)$, but lies along the radio source axis.

In our photoionization scenario there exists a direct cause and effect relationship between the radio ejecta and the ionization cone that leads to their alignment. It is possible to imagine that the nucleus was initially surrounded by a cloud opaque to ionizing radiation in all directions. When the radio jet turned on it plowed through the cloud and opened up a low density channel. As the radio lobes grew in size the increased density of the swept up gas at its outer edges allows it to effectively absorb the incident ionizing radiation from the central AGN which, in turn, can effectively escape along the cleared out, low density channel created by the radio source. If this is indeed the case, one might expect that the line-emitting gas would be edge-brightened on its radio source side due to the enhanced density along this interface. The intensity contours of our [O II]$\lambda3727$ map show the exact opposite; the eastern line-emission region has a higher surface brightness on the side facing away from the central axis of the radio source. If we assume that the gas of the eastern line-emission region wraps slightly around the bottom surface of a cylindrically shaped radio lobe (an interpretation consistent with the depolarization at this position), then the

brightening we perceive at the outer edge of the [O II] emission could be due to foreshortening. Instead of looking at a thin sheath of gas, as along the northern side of this line-emission region, we see a slightly greater column depth of gas at the bottom edge of this feature (see figure 8).

The evidence for directed radiation from a hidden nucleus provides supporting evidence for the 'unified models', that attempt to explain the relationships between active galaxies and quasars in terms of anisotropic emission and orientation effects (*e.g.* Barthel 1989; Antonucci 1993). The high redshift and very extended line-emission of 3C 34 makes this source an important example for this class of object. In light of this, it is important to ask the question why the morphology of the line-emission gas observed in 3C 34 is so different from the ionization cone-filling morphology common in Seyfert galaxies. The answer to this is twofold. First, we will use NGC 5252 (cz=6852 km s^{-1}) as a suitable comparison; it represents a well defined example of photoionization in Seyferts, and has the largest known ionization cone with a total extent of roughly 36 kpc. In our image of 3C 34 this would correspond to the first $2''.3$ on either side of the source and hence be well within the line-emission surrounding components A and B. At this inner position it may well be that the line-emitting gas fills the lateral extent of the ionization cone. Spatial resolutions better than $\sim 0''.4$ FWHM would be necessary to adequately resolve the warm gas this near to the central galaxy. An alternative explanation, however, along the lines of the 'unified models', would be that the ionization cones in both NGC 5252 and 3C 34 began in similar environments with both initial radio sources clearing out channels in the gas that eventually allowed the photoionizing radiation to escape. However, whereas the radio source in NGC 5252 has $P_{6cm} = 3.4 \times 10^{28}$ erg s^{-1}Hz^{-1}sr^{-1} and is very modest in size (Tadhunter & Tsvetanov 1989), 3C 34 is more than 10^4 more powerful at this wavelength. It is therefore plausible that only the considerably more powerful radio source in 3C 34 (and high redshift FR II radio galaxies in general) is capable of effectively sweeping out the IGM of its host source and confining the line-emission gas to its edges.

4.3. Alternative Interpretations

The ability of our photoionization model, in combination with radio source backflow and expansion, to explain the observed line-emission morphology and kinematics, does not guarantee that it is the only possible interpretation of 3C 34. We therefore feel obliged to account for possible alternative models, and discuss why we consider them to be inferior to our model in explaining our observational results.

4.3.1. Radio Source Collisional Excitation

The fact that the line-emission gas in 3C 34 extends great distances on either side of the central radio galaxy, the average overall alignment between the [O II] emitting gas and the radio source, and the general red-to-blueshift velocity trend across the source, would seem to point to

a direct collisional interaction between these two media. A closer look at a number of detailed features, however, can rule out this scenario as the main mechanism for ionizing the [O II] gas.

Although there does exists an overall red-to-blueshift trend in going from west to east in 3C 34, the velocity changes are abrupt and then remain almost constant across the length of the eastern line-emission region. Along the entire 70 kpc of this [O II] region the total velocity variation is less than $150 \, \mathrm{km \, s^{-1}}$ and is associated with moderate line widths of only about $250 \, \mathrm{km \, s^{-1}}$. This gives 3C 34 a velocity profile and line widths unlike those observed in powerful radio galaxies in which jet–cloud interactions are more obviously involved in creating the observed emission-line regions. At low redshifts examples of such sources include 4C 29.30, 3C 171, and PKS 2250–41 (van Breugel et al. 1986; Heckman et al. 1984; Clark & Tadhunter 1996), while for high redshifts 3C 352 and 3C 368 (Meisenheimer & Hippelein 1992; Hippelein & Meisenheimer 1992) are obvious candidates. In all of these sources the dynamical effect of the radio jet on the line-emitting gas is considerable with major axis velocity gradients of up to $1000 \, \mathrm{km \, s^{-1}}$ and line widths $\gtrsim$ $1000 \, \mathrm{km \, s^{-1}}$. A further characteristic of these radio source—ambient medium interaction objects is the relatively close correlation between the radio and line-emission morphologies. In 3C 34 this is obviously not the case, with the size of the radio source exceeding the regions of [O II] emission by more than a factor of two.

A critical test of a direct interaction between the radio source working surface and the gas that it excites and compresses are the implied cooling times. Assuming an angle between the line-of-sight and the radio source axis of 75° (Johnson et al. 1995), the deprojected flow velocity near component c would be $370 \, \mathrm{km \, s^{-1}} \times \cos^{-1}(75°) \simeq 1400 \, \mathrm{km \, s^{-1}}$. By relating the shock temperature to the temperature of the ambient external medium and the mach number of their highly supersonic model, Meisenheimer & Hippelein 1992 deduce an expression that relates the advance speed of the radio source bow shock (V_{bow}) to the temperature of the shock (T_{sh}),

$$V_{bow} = 0.28 \ \ T_{\mathrm{sh}}^{1/2} \quad \mathrm{km \, s^{-1}}. \tag{2}$$

Using this relationship we estimate that such a shock will heat the gas in 3C 34 to $T_{\mathrm{sh}} \sim 2.5 \times 10^7$ K. In terms of this temperature immediately behind the bow shock and the density n_c in the shocked gas clouds, the cooling time is given by

$$\tau_{\mathrm{cool}} = \frac{E}{|dE/dt|} \simeq 1.27 \, \frac{T_{\mathrm{sh}}}{n_c} \quad \mathrm{years}. \tag{3}$$

For the low metallicities expected for the IGM around high redshift radio galaxies and shock temperatures $\gtrsim 10^7$ K, we have assumed a constant cooling coefficient $\Lambda(T) \simeq 10^{-23} \, \mathrm{erg \, cm^3 \, s^{-1}}$ (Böhringer & Hensler 1989). Using a canonical ambient medium post-shock density of $n_c \sim 1 - 10 \, \mathrm{cm}^{-3}$ along with the derived shock temperature in equation 3, we can then compute the time required for the shocked plasma to cool to about 2×10^4 K. We find that $\tau_{\mathrm{cool}} \sim 3 \times 10^7 - 3 \times 10^6$ years are needed before this region can emit in its [O II]λ3727 line. The dynamical age of the interaction, however, as derived from the estimated shock velocity and the distance between component c and the radio source hotspot (d $\simeq$ 150 kpc), is on the order of 1×10^8 years. Thus,

with $\tau_{\mathrm{dyn}}/\tau_{\mathrm{cool}} \gtrsim 3 - 30$ for the eastern emission-line component the gas would have since cooled, and with the short radiative lifetime of its current line-emission luminosity (see below), cannot now be radiating the energy given to it by the radio source bow shock.

Of course, an alternative to a one-time energy injection could consist of secondary shocks driven into the cocoon surrounding the supersonic jet itself, or a more recent input of energy via the lateral expansion of the radio lobes. Although we cannot entirely discount such models, and it is certainly possible that some fraction of the excitation of the eastern line-emission region is due to collisional excitation by the radio lobe, the extremely quiescent velocity widths and large luminosity in this [O II] gas, are difficult to explain solely with this interpretation. For example, by assuming that the velocity dispersion of the [O II]λ3727 gas is representative of the material that constitutes the bulk of the ionized gas mass, the total kinetic energy of this medium will be of the order

$$E_k = 1 \times 10^{55} \; M_8 \; \sigma_{100}^2 \quad \text{erg}, \tag{4}$$

where M_8 is the mass of the ionized gas in the eastern region in units of 10^8 M$_\odot$, and σ_{100} is the total velocity dispersion in units of $100 \, \mathrm{km \, s^{-1}}$. For the eastern line-emission region we find M_{gas} $= 3.4 \times 10^8$. If we further assume that the observed radial line widths in this region are solely the result of turbulent motions in an isotropic system, $\sigma = \sqrt{3} \cdot 130 \, \mathrm{km \, s^{-1}}$. This means that the kinetic energy of the warm ionized gas is of the order of 2×10^{56} erg. Given the total luminosity of this region one derives a radiative lifetime of the line-emission gas of

$$\tau = 3 \times 10^4 \; \frac{E_{k\,56}}{L_{\mathrm{lines}\,44}} \; \epsilon \quad \text{years}, \tag{5}$$

where $E_{k\,56}$ is the kinetic energy in units of 10^{56} erg, $L_{\mathrm{lines}\,44}$ the luminosity of all the emission-lines in units of $10^{44} \, \mathrm{erg \, s^{-1}}$, and ϵ the efficiency factor in converting turbulence to line-emission. So, with conversion efficiencies ranging from 1 to 100% the dissipation time of the shock excited gas is only 140 to 1.4×10^4 years.

4.3.2.   *Photoionization by a Jet-Induced Starburst*

Since most high redshift radio galaxies have blue colours, perhaps indicative of large scale bursts of star formation, it has been suggested that the direct interaction between the outflow along the radio source axis and the IGM is the trigger for this phenomena (*e.g.* McCarthy et al. 1987 and Chambers et al. 1987). Although it is not a general phenomena, there is evidence that jet-induced star formation does indeed occur in low redshift sources such as Minkowski's object (van Breugel et al. 1985). Aside from providing a natural explanation for the radio/optical alignments, this model also provides a means of delivering ionizing radiation directly to the line-emitting gas. Therefore, the large extent of its line-emission region and its relatively close alignment to the radio axis makes 3C 34 a possible candidate for the jet-induced starburst scenario.

To see whether this model is compatible with our observations, we will use the spectral evolution models of Bruzual & Charlot 1993 to test whether the OB stars, produced by the passage of the radio source working surface, can provide a sufficient number of ionizing photons to *in situ* excite the surrounding line-emitting regions. For simplicity we have chosen an instantaneous burst model with a Salpeter initial mass function (IMF) (Salpeter 1955) that is weighted toward the high stellar mass end such that $2.5 \leq M \leq 125\ M_\odot$. Though extreme by comparison to other available models, the choice of an instantaneous starburst is made in order to provide the greatest amount of UV photons per stellar mass involved. The same is true for the choice of IMF and stellar mass range. Furthermore, the short duration of the radio source phenomena forces the need to convert the gas, shocked and compressed by the radio jet or its pressure cocoon, into stars in the shortest time possible. A maximum number of ionizing photons in the galaxy rest frame are created by this model at a time $\tau \sim 3.3 \times 10^6$ years after the initial burst. By integrating the resultant starburst spectrum blueward of the Lyα line we find that 5.1×10^{47} photons s^{-1} M$_\odot$$^{-1}$ are available to photoionize the ambient gaseous medium per solar mass of the starburst.

The [O II]$\lambda3727$ luminosities observed in the line-emission components B, a, b, and c, the likeliest sites for the location of an underlying starburst, can then be divided by this number to determine the minimum total mass of the starburst necessary to produce the required ionization. The computed masses range from 7×10^6 M$_\odot$ for component b, to 3×10^7 M$_\odot$ for source B. Barring extinction effects in the environment of the radio galaxy, which would undoubtably also affect the observed line-emission, these masses can be converted to observed flux levels by integrating the starburst spectrum over our the wavelength range sampled by our continuum filter ($\lambda_\circ=4033$Å ($\Delta\lambda_\circ=107$Å)). The resulting flux values have been converted to counts in this filter and added to our continuum image of 3C 34. Figure 9 shows these model starbursts to be very obvious at the positions of components B and c. (The more subtle enhancements at the positions of a and b are due to the weaker line-emission and pre-existing continuum at these positions). The absence of such obvious starburst continuum signatures in the original image (see figure 1b), near sources B and c, strongly excludes this model for the ionization of the line-emission regions in 3C 34.

5. Summary and Conclusions

Our morphological and kinematical study of 3C 34 favours a scenario in which the extended emission-line region is excited by the photoionizing UV radiation emitted by the central, hidden AGN. This model goes far in explaining the overall conical morphology of 3C 34's warm gas, and the detailed shapes of its individual [O II] knots. Furthermore, the energy budget necessary to excite this extended gas remains compatible with the central luminosity of typical 3C quasars at the same redshift. To account for the observed line-emission kinematics, however, requires an additional weak interaction between the radio lobes and the ambient medium. The large, quiescent, blueshifted velocity structure across the entire eastern region of 3C 34, as well as the redshifted velocity discontinuity of the western region, are best explained as gas swept aside by

the lateral expansion of the radio cocoon. This is corroborated by the spatial coincidence between the edges of the radio lobes and the [O II] gas, and by the radio depolarization at positions where this gas is in direct contact with the radio lobes. In this model the alignment of the [O II] region with the radio source arises from both emission signatures originating from the same central engine, and by the fact that the ionizing radiation preferentially escapes along an axis in which the ambient medium has been cleared by the radio source. The identification of 3C 34 with a cone of photoionization may be the first detection of such a feature in a high redshift, powerful radio galaxy. As such, this source can be an important link to the low redshift, low luminosity Seyfert galaxies in which such photoionization cones have traditionally been observed.

It should be noted that the line-emission morphology and kinematics of 3C 34 are unique in our current [O II] sample of 11 radio galaxies. This means that we cannot claim photoionization by a hidden, central AGN to be a general mechanism for exciting the line-emission regions observed in all powerful radio galaxies. In fact, at least two further means of ionization are necessary to explain the line-emission morphology and kinematics of all the sources in our sample: shock excitation of the ambient gaseous medium by an interaction with the radio source (Meisenheimer & Hippelein 1992; Hippelein & Meisenheimer 1992), and strong galaxy–galaxy interactions (Neeser et al. 1997). This argues against any universal, all-encompassing model for the alignment effect in powerful radio galaxies; a fact also supported by the need for both photoionization and radio source expansion and backflow to explain most aspects of 3C 34's line-emission regions.

A.   Photoionization by a Hidden AGN

A critical feature of a photoionization model is that the central AGN be able to provide a sufficient number of ionizing photons, to satisfy the total luminosity observed from the line-emission regions it is supposedly exciting. The number of ionizing photons emitted by the hidden AGN into a cone of solid angle, Ω_{beam}, and intercepted by a cloud at a distance R from the central source is,

$$\mathcal{N}_{\mathrm{ion}}(\nu) = \frac{A}{\Omega_{\mathrm{beam}} R^2} \int_{\nu_c}^{\infty} \frac{L_{\mathrm{ion}}(\nu)}{h\nu} \, d\nu. \tag{A1}$$

Here, $L_{\mathrm{ion}}(\nu)$ is the ionizing luminosity emitted by the AGN, A is the effective area of the cloud as seen from the AGN, and the integration is over all frequencies above the Lyman-continuum (ν_c). We assume that the ionizing radiation emitted by the central AGN obeys a non-thermal power-law of the form

$$L_{\mathrm{ion}}(\nu) = C\nu^{-\alpha} \qquad (\alpha > 0), \tag{A2}$$

where C is a constant and α is the spectral index of the far–UV energy distribution of the central source. Equation A2 can then be substituted into equation A1 and integrated such that,

$$\mathcal{N}_{\mathrm{ion}} = \frac{A C \nu_c^{-\alpha}}{\Omega_{\mathrm{beam}} R^2 h \alpha}. \tag{A3}$$

This number of 'expected' ionizing photons must then be compared with the 'observed' number of [O II]$\lambda3727$ photons emitted by the cloud, $\mathcal{N}_{\mathrm{[OII]}}$. However, to relate the incident radiation to the observed [O II]$\lambda3727$ line-emission we must take into account the ratio, k, of the number of ionizing photons required to produce one observed [O II]$\lambda3727$ photon. Furthermore, the effectiveness with which a given clump of gas absorbs incident photons is critically dependent on the covering factor, f_c — the fraction of the sky, as seen by the nucleus, covered by optically thick clouds. Combining these two factors we can then compute the effective number of ionizing photons impinging on the cloud, in terms of the observed number of [O II]$\lambda3727$ photons emitted by the cloud,

$$\mathcal{N}_{\mathrm{eff}} = \frac{k}{f_c} \frac{L_{\mathrm{[OII]}}}{h\nu_{\mathrm{[OII]}}}. \tag{A4}$$

Comparing equations A4 and A3 and solving for the constant C, which is then introduced into equation A2 gives the monochromatic luminosity that the hidden AGN must emit to produce the observed line-luminosity,

$$L_{\mathrm{ion}}(\nu) = \frac{k}{f_c} \frac{L_{\mathrm{[OII]}}}{h\nu_{\mathrm{[OII]}}} \frac{\Omega_{\mathrm{beam}} R^2 h \alpha}{A} \left(\frac{\nu}{\nu_c}\right)^{-\alpha}. \tag{A5}$$

Most critical for this photoionization model will be those emission-line components that have the highest surface brightness and lie furthest from the central source. But, before this equation can be applied to these sources a number of further assumptions must be made about the variables in this expression. For simplicity, we will assume that the projected area of the [O II]

sources (clouds) is similar to the actual total area facing towards the continuum source, with a circular cross-section having a characteristic radius (r) of one-half the knot's FWHM. We must also consider what fraction of the ionizing radiation goes into producing the observed [O II]$\lambda3727$ flux. Assume that the environment of our radio galaxies can be approximated by the radiative transfer properties in a giant extragalactic HII region, we can use the model results of Stasinska 1980. Using parameters typical of the line-emission gas observed in our sources; a temperature of T_{eff}=4.5 × 10^4, a metal abundance relative to solar of $Z/Z_\odot \lesssim 0.2$, and interpolating between the computed densities $10 < n_e < 100$ cm^{-3}, this model gives an [O II]$\lambda3727$ to $H\beta$ ratio of 1.5. For case B recombination, the ratio of the number of $Ly\alpha$ to $H\beta$ photons is 8.5 (Osterbrock 1989). Therefore, we estimate that the number of photoionizing photons required for every [O II]$\lambda3727$ photon produced is $k \sim 6$. Finally, we will assume a spectral index of $\alpha = 1$ (Villar-Martin et al. 1997).

With these assumptions in place, equation A5 can be used to compute the *required* luminosity that the ionizing source must have in order to produce the observed [O II]$\lambda3727$ flux. By integrating this expression with respect to ν, over any filter of interest that covers a rest frame wavelength range of $\lambda_1 < \lambda < \lambda_2$, we can determine the broad–band luminosities the AGN must produce. In this way the required luminosity can be simplified to contain only those parameters specific to an individual source,

$$L_{\mathrm{ion}}^\lambda = 24.5 \ L_{\mathrm{[OII]}} \ \frac{\Omega_{\mathrm{beam}} R^2}{f_c A} \ ln\left(\frac{\lambda_2}{\lambda_1}\right) \quad \mathrm{erg \, s}^{-1}. \tag{A6}$$

This, in turn, can be converted to expected apparent magnitudes if the ionizing beam from the hidden ionizing source were directed toward us. The resulting luminosity and magnitude can then be compared with values from known 3CR quasars at redshifts similar to that of 3C 34. Since the 'unifying schemes' assume radio galaxies to differ from quasars primarily in terms of orientation, the luminosity that we compute to be necessary to photoionize the observed line-emission, must be less than or equal to those observed for the intrinsically brightest quasars.

REFERENCES

Allington-Smith, J. R. 1984, MNRAS, 209, 665

Antonucci, R. 1993, Ann. Rev. Astron. Astrophys., 31, 473

Barthel, P. D. 1989, ApJ, 336, 606

Böhringer, H., & Hensler, G. 1989, A&A, 215, 147

Bruzual, G. A., & Charlot, S. 1993, ApJ, 405, 538

Burstein, D., & Heiles, C. 1982, AJ, 87, 1165

Chambers, K. C., Miley, G. K., & van Breugel, W. 1987, Nature, 329, 604

Clark, N. E., & Tadhunter, C. N. 1996, Cygnus A – Study of a Radio Galaxy, ed. C. L. Carilli & D. E. Harris, Cambridge University Press, 15

Dressler, A., & Gunn, J. 1992, ApJS, 78, 1

Garrington, S. T., Conway, R. G., & Leahy, J. P. 1991, MNRAS, 250, 171

Heckman, T. M., Baum, S. A., van Breugel, W. J. M., & McCarthy, P. J. 1989, ApJ, 338, 48

Heckman, T. M., van Breugel, W. J. M., & Miley, G. K. 1984, ApJ, 286, 509

Hippelein, H., & Meisenheimer, K. 1992, A&A, 264, 472

Jenkins, C. J., Pooley, G. G., & Riley, J. M. 1977, Mem. R. Astron. Soc., 84, 61

Johnson, R. A., Leahy, J. P., & Garrington, S. T. 1995, MNRAS, 273, 877

McCarthy, P. J., van Breugel, W., Spinrad, H., & Djorgovski, S. 1987, ApJ, 321, L29

McCarthy, P. J., Spinrad, H., & van Breugel, W. 1995, ApJS, 99, 27

McCarthy, P. J., Baum, S. A., & Spinrad, H. 1996, ApJS, 106, 281

Meisenheimer, K., & Hippelein, H. 1992, A&A, 264, 455

Neeser, M. J., Hippelein, H., & Meisenheimer, K. 1997, in prep

Neff, S. G., Roberts, L., & Hutchings, J. B. 1995, ApJS, 99, 349

Osterbrock, D. E. 1989, *Astrophysics of Gaseous Nebulae & Active Galactic Nuclei*, University Science Books

Prieto, M. A., Walsh, J. R., Fosbury, R. A. E., & di Serego Alighieri, S. 1993, MNRAS, 263, 10

Rawlings, S., Eales, S., & Lacy, M. 1991, MNRAS, 251, 17P

Riley, J. M., Longair, M. S., & Gunn, J. E. 1980, MNRAS, 192, 233

Röser, S., & Bastian, U. 1991, PPM Star Catalogue, Spektrum, Akademischer Verlag, Heidelberg.

Salpeter, E. E. 1955, ApJ, 121, 161

Spinrad, H. 1982 PASP, 94, 397

Spinrad, H., Djorgovski, S., Marr, J., & Aguilar, L. 1985 PASP, 97, 932

Stasinska, G. 1980, A&A, 84, 320

Tadhunter, C. N., & Tsvetanov, Z. I. 1989, Nature, 341, 422

van Breugel, W. J. M., Filippenko, A. V., Heckman, T. M., & Miley, G. K. 1985, ApJ, 293, 83

van Breugel, W. J. M., Heckman, T. M., Miley, G. K., & Filippenko, A. V. 1986, ApJ, 311, 58

Villar-Martin, M., Tadhunter, C., & Clark, N. 1997, A&A, in press

Wilson, A. S., & Tsvetanov, Z. I. 1994, AJ, 107, 1227

Fig. 1.— Labelled components of 3C 34 as discussed in text. (a) Continuum subtracted [O II]λ3727 image. (b) Line-free continuum image with a rest-frame wavelength of $\lambda_\circ$=4033Å ($\Delta\lambda_\circ$=107Å). The first contours are at 2.5σ above the mean background level, while subsequent contours are at levels of 1.5nσ. For all images presented, north is at the top and east is to the left, and the centroid of continuum component A defines the origin.

Fig. 2.— A logarithmic grayscale representation of the line-emission (top panel) and continuum (bottom panel) images of 3C 34. The 20 cm radio contour map of Neff et al. 1995, whose spatial resolution of 1″4 FWHM beam is comparable to that of our images, is superimposed on the [O II] frame. The line-emission image consists of the sum of 18 Fabry-Perot frames obtained across the line profile. The continuum image has a rest-frame wavelength of $\lambda_\circ$=4033Å ($\Delta\lambda_\circ$=107Å).

Fig. 3.— Intensity cross-sections of 3C 34. The top three panels show the [O II] line-emission for the three major regions of this source; the eastern emission-line region (components b and c), the central section (components A and B), and the western region (component a). The bottom panel shows the continuum profiles of component A and a nearby star (dotted line). The three cross-section cuts, east, center, and west, are shown in the inset line-emission contour plot. All positions are given as straight-line distances from the central continuum peak. It should be noted that the x-axis distance scale of each plot, with the exception of the central continuum and line-emission plots, are different from one another. Also, the smoothness of these curves is partly due to the rebinning of the data, such that only every second data point is independent.

Fig. 4.— [O II] line profiles at the positions of the major components labelled in figure 1, and at the diffuse emission between components b and c (b-c). Each profile is an average over 4×4 pixels in units of counts per pixel above the continuum.

Fig. 5.— A colour representation of the radial velocities (top panel) and the deconvolved velocity widths (bottom panel) of the [O II]λ3727 line-emission in 3C 34. The axes are labelled in arc seconds from the origin defined by the optical continuum emission peak A (shown with a cross). At the bottom of each panel a gradient scale is given matching the diagram's colours to velocities in km s^{-1}. On the velocity map we also show the axes used for the cross-sections given in figure 6. The lengths of the cuts are given in figure 3.

Fig. 6.— The velocity profiles (top panels) and the deconvolved velocity widths (bottom panels) along three major axis cuts of 3C 34. The three panels for each of velocity and FWHM are divided into the eastern, central, and western regions defined in figure 3. The position and velocity origin has been taken to be at the radio galaxy center (component A).

Fig. 7.— Our proposed photoionization cone superimposed on the grayscale [O II] image of 3C 34. The dashed line indicates the radio source axis, as measured from the outermost hotspots of the 20 cm map shown in figure 2. The apex of the cone is located at the position of the central continuum source A; the location of the hidden AGN. An opening angle of 60° is the minimum required to photoionize the observed line-emission.

Fig. 8.— A schematic view perpendicular to the line-of-sight to 3C 34, looking *into* the eastern radio lobe of this source. In our model, the gas of the eastern line-emission region has been swept up by the southern end of the expanding radio lobe. The greater column depth along our line-of-sight to the bottom of the line-emission region results in a higher [O II] surface brightness on the outer side of this feature.

Fig. 9.— An **artificial** continuum image of 3C 34 as it would appear if each of the line-emission components were the result of an underlying starburst. Each starburst has been marked with the label corresponding to its associated line-emission component. With the exception of components a and b, in which continuum emission exists in the original image, components B and c are prominent and located in regions previously devoid of comparable continuum emission. Each starburst was given the same PSF as its associated line-emission component. This contour map should be compared with the observed continuum image shown in figure 1b.

Table 1: Properties of 3C 34 Continuum and [O II]λ3727 Components

comp.	rel. pos. $\Delta\alpha$	$\Delta\delta$	r^a kpc	redshift	m_{4033}	M_{4033}	f([O II]λ3727)^b (R$_{aperture}$)	FWHM^c Å
All	—	—	—	0.689	—	—	223 (9.6)	38.7
A	0$''$0	0$''$0	0.0	0.6900±0.0007	20.68	-22.7	62.3 (1.8)	17.6
B	1$''$4	1$''$3	15.3	0.6899±0.0007	—	—	45.3 (1.6)	18.7
C	0$''$5	4$''$3	34.5	—	21.67	-21.7	—	—
a	-4$''$3	0$''$1	34.1	0.693±0.001	—	—	18.6 (1.4)	19.5
b	3$''$6	-1$''$1	30.1	0.687±0.001	—	—	12.3 (1.4)	14.4
c	7$''$1	-3$''$1	61.4	0.6881±0.0008	—	—	29.4 (1.9)	12.6

^{a} H$_\circ$=50 km s^{-1} Mpc^{-1} q$_\circ$=0.5
^{b} flux in units of 10^{-16} erg s^{-1}cm^{-2}(radius of aperture in arcsec)
^{c} observed FWHM corrected for instrumental broadening

Table 2: Results of Photoionization Calculations for 3C 34

Source	Dist from AGN (")	Cone Opening Angle	Cloud Radius (")	L$_B$ AGN (erg s^{-1})	m$_v$ AGN
B	1.9	60°	1.02	1.4×10^{44}	19.5
			1.60	9.3×10^{43}	20.0
		88°	1.02	2.8×10^{44}	18.8
			1.60	1.8×10^{44}	19.3
c	8.2	60°	1.20	1.1×10^{45}	17.3
			1.90	8.0×10^{44}	17.6
		88°	1.20	2.2×10^{45}	16.5
			1.90	1.5×10^{45}	16.9